Received: 13 April 2021 | Revised: 6 July 2021 | Accepted: 27 July 2021

DOI: 10.1002/cjce.24291

THE CANADIAN JOURNAL OF CHEMICAL ENGINEERING

Canadian Society for Chemical Engineering | *For Our Future*
Société canadienne de génie chimique | *Pour notre avenir*

MINI-REVIEW

Experimental methods in chemical engineering: X-ray absorption spectroscopy—XAS, XANES, EXAFS

Ana Iglesias-Juez[1] | **Gian Luca Chiarello**[2] | **Gregory S. Patience**[3] | **M. Olga Guerrero-Pérez**[4]

[1]Instituto de Catálisis y Petroleoquímica, CSIC, Madrid, Spain

[2]Dipartimento di Chimica, Università degli Studi di Milano, Milan, Italy

[3]Chemical Engineering, Polytechnique Montréal, Montréal, Québec, Canada

[4]Departamento de Ingeniería Quimica, Universidad de Málaga, Málaga, Spain

Correspondence
M. Olga Guerrero-Pérez, Departamento de Ingeniería Quimica, Universidad de Málaga, E-29071-Málaga, Spain.
Email: oguerrero@uma.es

Funding information
Canada Research Chairs, Grant/Award Number: 950-231476

Abstract

Although X-ray absorption spectroscopy (XAS) was conceived in the early 20th century, it took 60 years after the advent of synchrotrons for researchers to exploit its tremendous potential. Counterintuitively, researchers are now developing bench type polychromatic X-ray sources that are less brilliant to measure catalyst stability and work with toxic substances. XAS measures the absorption spectra of electrons that X-rays eject from the tightly bound core electrons to the continuum. The spectrum from 10 to 150 eV (kinetic energy of the photoelectrons) above the chemical potential—binding energy of core electrons—identifies oxidation state and band occupancy (X-ray absorption near edge structure, XANES), while higher energies in the spectrum relate to local atomic structure like coordination number and distance, Debye-Waller factor, and inner potential correction (extended X-ray absorption fine structure, EXAFS). Combining XAS with complementary spectroscopic techniques like Raman, Fourier transform infrared (FTIR), X-ray photoelectron spectroscopy (XPS), and electron paramagnetic resonance (EPR) elucidates the nature of the chemical bonds at the catalyst surface to better understand reaction mechanisms and intermediates. Because synchrotrons continue to be the light source of choice for most researchers, the number of articles Web of Science indexes per year has grown from 1000 in 1991 to 1700 in 2020. Material scientists and physical chemists publish an order of magnitude articles more than chemical engineers. Based on a bibliometric analysis, the research comprises five clusters centred around: electronic and optical properties, oxidation and hydrogenation catalysis, complementary analytical techniques like FTIR, nanoparticles and electrocatalysis, and iron, metals, and complexes.

KEYWORDS

EXAFS, operando, synchrotron, XANES, XAS

1 | INTRODUCTION

The Würzburg Physical-Medical Society's journal (1895) published Wilhelm Röntgen's experimental observations entitled 'On a new kind of ray: A preliminary communication'.[1] In that year, Röntgen recorded the famous photograph of his wife's hand with shadows formed by the bone, her wedding ring, and the penumbra of the flesh. Since the nature of this radiation was unknown, they called it X-rays, which we now recognize as electromagnetic waves with wavelengths shorter than UV and longer than γ, that is, ranging from 0.025 to 25 Å (0.0025–2.5 nm) corresponding to energies, according to the Planck's law, from 0.5 to 500 keV.

X-ray absorption spectroscopy (XAS) comprises both X-ray fluorescence (XRF) and X-ray absorption fine spectroscopy (XAFS) with photon energies above 5 keV (hard X-rays). XAFS, in turn, includes X-ray absorption near-edge structure (XANES, also known as near-edge X-ray absorption fine structure—NEXAFS) and extended X-ray absorption fine structure (EXAFS). High vacuum beamlines, which minimize X-ray absorption by air, also apply soft X-rays, especially for elements lighter than titanium and less energetic edges like M-edges of metals. Maurice de Broglie (older brother of Louis) pioneered X-ray spectroscopy and measured the first absorption edges (Ag and Br K-edges) in 1913. However, it was obvious that practical application would require more brilliant polychromatic X-ray sources, better detectors, and a theoretical framework to interpret the signals. For this reason, advances in XAFS coincide with that of synchrotron light sources. Over half a century after Röntgen's discovery, researchers at Cornell recorded X-ray absorption spectra with synchrotron radiation for the first time.[2] High quality complete EXAFS spectra were recorded 20 years later together with the development of modern theory and FT of EXAFS.[3,4]

XAFS has become a very powerful analytical tool that researchers apply in chemistry, homogeneous and heterogeneous catalysis, molecular and condensed matter physics, materials science, engineering, earth science, biology, and protection of cultural heritage. Of the close to 5000 articles indexed by WoS from 2018 to mid-2020, half were in physical chemistry and multidisciplinary materials science but only 286 were in chemical engineering. Other scientific categories that overlap with chemical engineering research include multidisciplinary chemistry (ranked 4th with 640 articles), environmental sciences (5th, 499 articles), and nano-science and nanotechnology (7th, 471 articles).[5] The main advantage of XAFS is that it is element specific and sensitive to the oxidation state and local (fine) structure (i.e., it reveals short-range order) as compared to X-ray diffraction (XRD), which is sensitive to long-range structural order.[6] Hence, contrary to XRD, scientists apply XAFS to characterize amorphous materials, highly disordered systems, and liquid solutions. This article is part of a series dedicated to experimental methods in chemical engineering.[7] Each article first introduces the theory, describes the instrumentation, and highlights applications, with a particular emphasis on chemical engineering. Finally, this tutorial review mentions uncertainties and limitations of the method and identifies areas of future research.

2 | THEORY

The probability that matter absorbs X-ray energy (E) is proportional to its density, ρ, and the ratio of its atomic number and E to the cubed $\rho Z^3/E^3$. This property forms the basis of X-ray imaging techniques—computed tomography, radiography, and baggage scanners of airport security. Because X-ray absorption increases with the cube of Z, tissue light elements, C, H, N, and O ($Z \leq 8$), absorb less than bones, which is predominantly Ca ($Z = 20$). Radiography generates Z contrast images based on this property. Sample thickness, t, and the absorption coefficient, μ, are two other factors that dictate how much radiation passes through, I—the intensity of transmitted X-rays. According to the Lambert–Beer law, I is proportional to the incident beam X-ray, I_0, and the exponential of the product of μ and t:

$$I = I_0 \exp(-\mu t) \tag{1}$$

Spectroscopic techniques measure the interaction between electromagnetic radiation and matter. In UV–Vis spectroscopy, valence electrons of the outermost shell of atomic or molecular orbitals absorb this energy.[8] In infrared spectroscopy, molecules absorb photons with an energy equal to one of its vibrational frequencies—a transition between electronic states.[9] In XAS, energetic hard X-rays eject electrons of the tightly bound core electrons occupying the innermost orbitals (Figure 1, left panel). The energy required to remove an electron from an atom equals the binding energy, E_0, which is 4966 eV for the 1s K shell of Ti and increases exponentially with Z to 88 005 eV for Pb. The energy to eject Pb core electrons at the L_3 and M_5 shells is 13 035 eV and 2484 eV, respectively, which is much lower than for the 1s electron. X-ray absorption spectra come from the K-edge (particularly for lighter elements), and the L- and M-edges (Figure 1, right panel). The same power law function fits each of the K, L_3, and M_5 shells ($R^2 > 0.995$):

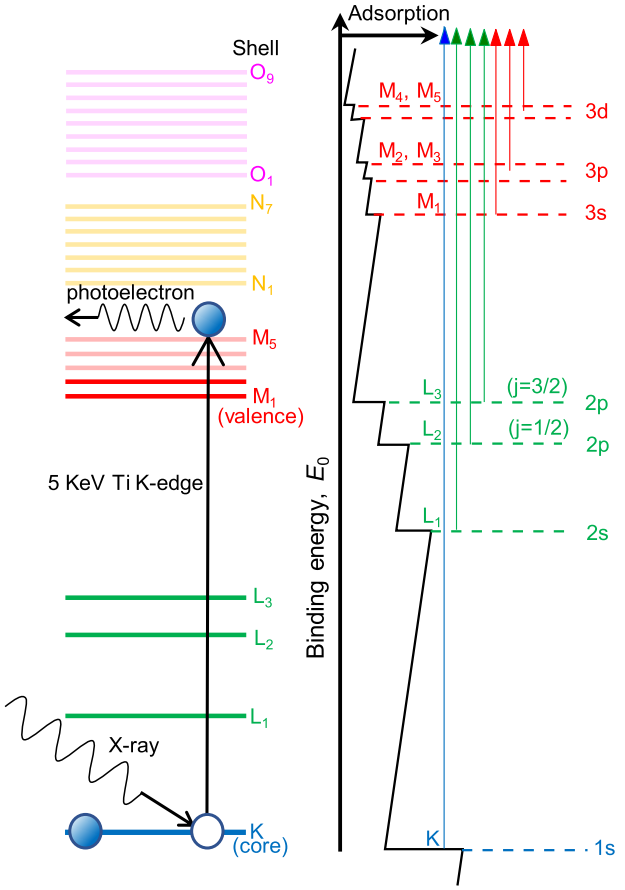

FIGURE 1 Left panel: Ti 1s K-shell electron absorption of an X-ray photon (5 keV) followed by the photoelectron ejection out of the absorber atom into the continuum. Adapted from Patience.[10] Copyright 2017 Elsevier. Right panel: Core electron excitation from K, L, and M band edges. Adapted from Atenderholt (CC BY-SA 3.0 [http://creativecommons.org/licenses/by-sa/3.0])[11]

$$E_0(\mathrm{K}) = 0.001\,16(Z+8)^{2.5} \quad \sigma_{n=11} = 0.3 \text{ keV} \tag{2}$$

$$E_0(\mathrm{L_3}) = 0.000\,18(Z+8)^{2.5} \quad \sigma_{n=9} = 0.09 \text{ keV} \tag{3}$$

$$E_0(\mathrm{M_5}) = 0.000\,044(Z+8)^{2.5} \quad \sigma_{n=6} = 0.07 \text{ keV} \tag{4}$$

The binding energy of 1s K shells, $E_0(Z)$, is over 6 times that of the L_3 shells, which in turn are 4 times greater than that of the M_5 shells (Figure 2).

The XAS community uses both μ and A (absorbance) interchangeably to measure X-ray absorption intensity as a function of the incident photon energy, E. In UV–Vis spectroscopy, ϵ is equivalent to μ and the optical length and concentration contribute to absorbance. In solid state chemistry, μ is the absorbance of a sample of unit thickness and unit optical length at a given energy. The absolute intensity depends on sample density, loading (mass fraction), and thickness: A 5% Pt/Al_2O_3 sample absorbs

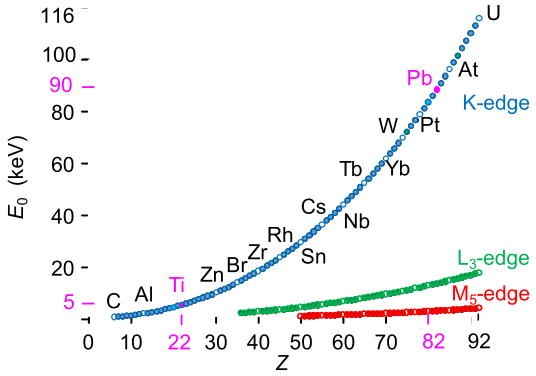

FIGURE 2 Electron binding energy, E_0, as a function of atomic number, Z for K, L3, and M5 shells. The binding energy for Ti is about 5 keV and 90 keV for Pb. Adapted from Patience.[10] Copyright 2017 Elsevier

more than a 1% Pt/Al_2O_3 at the Pt L3-edge. So, XAS detects changes in atomic concentration; however, ICP (inductively coupled plasma), XPS (X-ray photoelectron spectroscopy), XRF, and EDX (energy dispersive X-ray spectroscopy) cost and efforts are less compared to XAS measurements in a synchrotron. XAS does measure changes in oxidation state and chemical environment quantitatively. The XAS spectrum is normalized between the pre-edge and the post-edge line in order to remove the sample concentration, density, and thickness dependency of the edge jump intensity and to allow quantitative comparison and analysis of spectra of different materials (including reference) independently of the experimental conditions and chemical composition and concentration. The normalization thus confounds μ and A.

XAS spectra are plots of μ-absorbance, as a function of X-ray photon energy (Figure 3) in the region of the selected binding energy (E_0).[12] Because E_0 depends on the atomic number, it turns out that XAS is element specific. A full XAS spectrum is usually measured between 150 eV below E_0 and up to 1000 eV above E_0. An XAS spectrum includes the XANES (which is the same as NEXAFS), and the EXAFS (Figure 3). XANES comprises the pre-edge with small features between the Fermi energy and threshold, edge (edge jump = $\Delta\mu_0[E]$, where the incident energy equals the binding energy that ejects a core electron into the continuum), and near-edge. In the latter, the excess energy becomes kinetic energy with a photoelectron—a wave that propagates away from the absorber atom. The XANES spectra and EXAFS are mathematically processed independently; the former identifies oxidation state and d-band occupancy while the higher energies in the spectrum (EXAFS) relate to the local chemical environment surrounding the absorber atom like coordination number (number of atomic

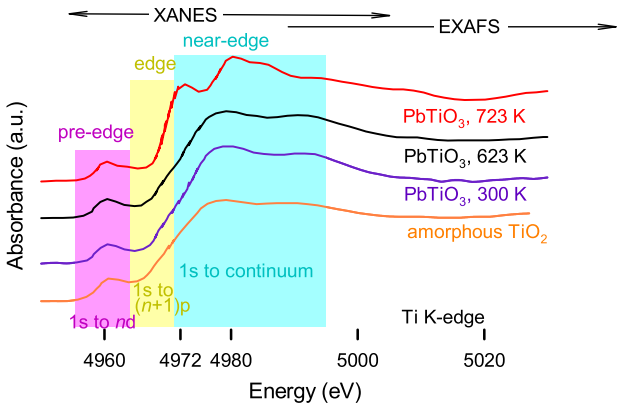

FIGURE 3 X-ray absorption spectroscopy (XAS) spectra at the Ti K-edge of $PbTiO_3$ thin film as a function of calcination temperature. The local structure of the Ti atoms is close to amorphous TiO_2 up to 623 K (the lowest curve). At 723 K, the spectra is practically identical to a reference $PbTiO_3$ (not shown), which confirms all the TiO_2 reacted. Adapted from Holgado et al.[12] Copyright 2017 Elsevier

ligands) and distance, Debye-Waller factor, and inner potential correction.

3 | DESCRIPTION

3.1 | XAS experimental setup

Synchrotrons had been the only source of polychromatic X-rays for XAS. Recent advances in bench top spectrometers like line focus X-ray tubes and plasma X-ray sources are now available. The applications for these instruments, which are much less costly than synchrotrons, include monitoring catalyst stability, which requires extended run times, and hazardous materials.[13] Synchrotrons produce an electron beam and then accelerate them and inject them into ultra-high vacuum storage rings in which they circulate at velocities approaching the speed of light, c. Bending magnets, undulators, and wigglers located along the storage ring perturb the beams trajectory that provokes the emission of photons (i.e., the synchrotron light). Because the electron beams travel at close to c, they are subjected to the Doppler effect and the Lorentz contraction of distances. Both relativistic phenomena shrink the emitted photon's wavelength (infrared to hard X-rays) into the laboratory frame compared to the emitting electron frame.[14] The emitted synchrotron light is delivered to the beamlines which are located tangentially to the storage ring in correspondence of each light source (bending magnet, undulator, or wiggler). A synchrotron facility comprises several beamlines along which the experimental laboratories are built for the specific application (Figure 4).

A common XAS configuration comprises the focusing mirrors, monochromators, higher harmonic rejection mirrors, ionization chambers, and sample cells that operate at experimentally relevant conditions (in-situ and *operando* experiments). Samples are loaded between the first and second ionization chamber while the reference metal foil of the investigated element for calibration goes between the second and the third. Ionization chambers are cylinders filled with He, N_2, Kr, Xe, Ar, or mixtures of them that measure the intensity of the incident radiation, I_0, and transmitted light, I, passing through the sample. Rotating the double monocrystal X-ray monochromator changes the incident angle, θ, to scan the X-ray energies. The X-ray diffraction obeys Bragg's law, which states that the product of an integer n and the wavelength λ equals the product of the distance between two lattice planes d and the $\sin\theta$, where θ is measured normal to the surface:

$$n\lambda = 2d\sin\theta. \tag{5}$$

For higher energy X-rays, researchers substitute the Si(111) with a crystal with higher Miller index such as Si(211), Si(311), Si(220), and Si(511). To reject higher X-ray harmonics ($n > 1$), the second monocrystal is slightly detuned or uses mirrors, or a combination of the two. To determine the adsorption coefficient, we rearrange Equation (1) to express μ as a function of t and I_0 and I:

$$\mu = \frac{1}{t}\ln\frac{I_0}{I} \tag{6}$$

XAS can be measured both in transmission or in fluorescence mode. Indeed, the electron hole generated after the ejection of a core electron can be filled by relaxation of higher energy electron core-level with emission of an X-ray photon by fluorescence. For example, relaxations from an L_3 or an L_2 shell to the K shell of copper leads to the emission of the characteristic K_1 (8046.3 eV corresponding to 1.5409 Å) and K_2 (8026.7 eV corresponding to 1.5446 Å) radiations. Core hole generation and consequent relaxation processes are proportional to the incident X-ray intensity. Thus, the absorption coefficient μ can be derived indirectly from the intensity of fluorescence X-rays (I_f), as $\mu \propto I_f/I_0$. In the latter mode, the sample is placed at 45° with respect to the incident X-ray beam, facing a fluorescence detector (typically silicon or germanium semiconductor detectors). Fluorescence is element specific, because the detector is tuned to count only the emitted X-rays of specific energy, that is, of characteristic energy of the investigated

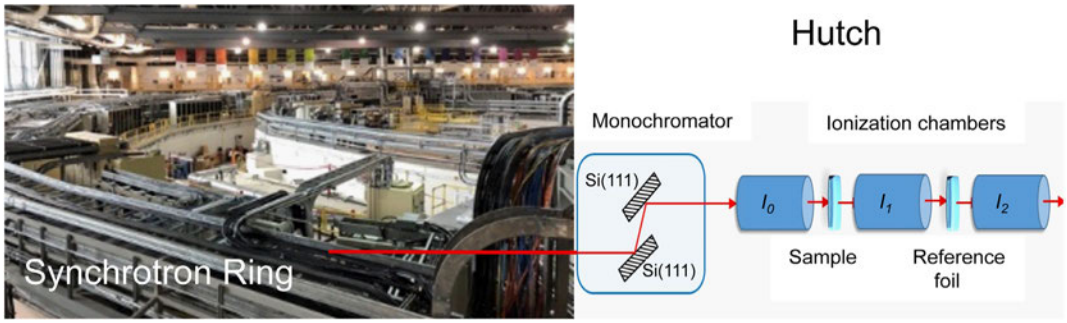

FIGURE 4 The photo to the left is the Canadian Light Source in Saskatoon that accelerates electrons and directs the synchrotron light into beamlines that lead to dedicated monochromatic in hutches that shine on samples, reference materials, and ionization chambers

element. Thus, fluorescence is particularly useful for thick samples where the transmitted intensity is too low or for diluted species into a high absorbing matrix (e.g., 0.01 gg^{-1} Pd supported on CeO_2) in order to identify the contribution of the element under investigation. In contrast, fluorescence is unsuitable for time resolved measurements because of the longer acquisition time of the fluorescence detector with respect to the ionization chamber.

3.2 | Near edge structure—XANES

X-ray energies of the XANES spectrum around the absorption edge range from −50 eV below E_0 to 100 eV above E_0. Oxidation state, the coordination environment of the absorber atom, and ligand type chemistry impact the edge position and shape of the XANES spectrum. Below the absorption edge the spectrum is linear and smooth; it increases sharply at the edge (jump), and then oscillates beyond it. In early photographic emulsion detectors, the intense peak at the edge was a bright white line and so researchers adopted this terminology.

Photoelectric transitions change the azimuthal quantum number l to $l \pm 1$ (selection rules). For example, X-ray radiation absorption promotes a K shell $(l = 0)$ electron into np discrete electronic states and the continuum. However, the $1s \rightarrow nd$ is forbidden as in this case $l = 2$. The p band of transition metals are filled while the d levels are unfilled. However, p-d hybridization of the O 2p and metal d levels creates accessible molecular orbital states. The allowed states are at the origin of pre-edge features—isolated peaks and shoulders (Figure 3).

Cu_2O tetrahedral coordination favours hybridization; consequently, the pre-edge peak is intense but the octahedral coordination of CuO is symmetrical, so $s \rightarrow d$ transitions are forbidden and weak.[15] The L3-edge X-ray absorption white line of transition metals is essentially due to the $2p_{3/2} \rightarrow$ d transition (the contribution of the $p \rightarrow s$ transition is 50 times weaker).[16] However, according to the ligand field theory (LFT), the five degenerate d-orbitals split into three lower energy orbitals, t_{2g}, and two higher energy orbitals, e_g, in octahedral coordination. This splitting generates the appearance of two peaks in the white line that overlap depending on the extent of the $t_{2g} - e_g$ energy splitting (i.e., on the symmetry of the coordination unit).[17] Hence, a XANES spectrum identifies the oxidation state as the position of the edge of the absorber atom varies linearly with oxidation state.

We apply XANES for in-situ experiments to follow: for example, the temperature programmed reduction (TPR) profile of a metal oxide or to explore catalyst redox dynamics *operando*. With this information, we can identify the optimal catalyst pre-treatment conditions and characterize reaction mechanisms. For example, 723 K is sufficient to form $PbTiO_3$ and not 623 K (Figure 3). Because hard X-rays penetrate deeply, XAS is essentially a bulk technique and the spectra are a linear combination of all the chemical forms of the selected element inside the sample. Therefore, we require spectra of reference materials to complement the analysis. For example, the fraction of TiO_3 in the mixture is a linear combination of the spectra of the pure TiO_2 and $PbTiO_3$ references. Quantitative approaches simulate XANES spectra with ab initio theoretical calculations with dedicated programs such as FEFF9 and FDMNES.[18–20]

3.3 | Extended fine structure—EXAFS

The kinetic energy, E_k, of photoelectrons ejected from the absorber atom equals the excess energy $(E - E_0)$. The wavelength of a particle, λ, is the ratio of Planck's constant, h, to its momentum, p: $\lambda = h/p$. The de Broglie hypothesis holds that the photoelectron wavenumber, $k = 2\pi/\lambda$, is the ratio of particle momentum and the reduced Planck's constant $(\hbar = h/2\pi)$, $k = p/\hbar$. The product of electron mass and velocity is momentum $p = m_e u$ and $E_k = 1/2 m_e u^2$. Thus, we have the following:

$$E_k = \frac{p^2}{2m_e} = E - E_0 \quad (7)$$

With the de Broglie hypothesis, we rearrange this equation to express photoelectron wavenumber as a function of the incident X-ray energy:

$$k = \sqrt{\frac{2m_e(E-E_0)}{\hbar^2}} \quad (8)$$

Whereas XANES interprets the near edge signal of the XAS spectrum, EXAFS considers the signal from about 50 eV up to 1000 eV beyond E_0. The EXAFS spectrum of a single atom in total vacuum is a smooth line with an absorbance of $\Delta\mu_0$, that is, the edge jump corresponding to the difference between the post- and the pre-edge lines. Practically, photoelectrons are back scattered by surrounding atoms (coordination environment) that are at the origin of oscillations in the XAS spectrum.

Absorbing atoms and nearby scattering atoms act like a type of interferometer. When the wavelength of the photoelectron is an integer of the interatomic distance (path length), there will be constructive interference. Because μ represents the probability that X-rays are absorbed, at X-ray energy below the electron binding energy, the probability of X-ray absorption is low (i.e., low $\mu(E)$) because electron transitions are unlikely (impossible). On the other hand, at energy above it, the probability of X-ray absorption is high due to the allowed electron transition, and $\mu(E)$ rises up. In the EXAFS region, the absorbance reaches a maximum in the case of constructive interference, when the scattered photoelectron waves are in phase, and a minimum for destructive interference, when they are out of phase. Because the photoelectron wavenumber k ranges from 0 up to 16 $Å^{-1}$, the in- phase event can occur several times, thus originating likewise oscillations in the EXAFS spectrum.

$\chi(E)$ is the normalized EXAFS function in the incident X-ray energy domain, and it equals to the difference between the measured absorbance $\mu(E)$ and the single atom absorbance (spline) $\mu_0(E)$ divided by the jump in absorbance at the edge $\Delta\mu_0$:

$$\chi(E) = \frac{\mu(E) - \mu_0(E)}{\mu_0} \quad (9)$$

In the following step, we convert the abscissa from energy to wavenumber k (Equation 8) to give $\chi(k)$, which only shows the oscillatory part of the original XAS spectrum. The amplitude of the oscillations decrease with increasing k. Each $\chi(k)$ value is multiplied by the corresponding k^n with n equal to 2 or 3 to compensate for this phenomenon, known as k weighting.

As photoelectrons propagate outward in all directions, they follow several scattering paths, i (Figure 5), all of which contribute to the EXAFS spectrum (Table 1). The backscattered electron interacts as in the case of an interferometer by combining waves. When the electron wavelength (that changes with increasing incident X-ray energy) is an integer of the path length (i.e., approximately the interatomic distance), you have constructive interference that increases the probability of X-ray absorption and therefore of $\mu(E)$:

$$\chi(k) = \sum_i \frac{(N_i S_0^2) F_i(k)}{kR_i^2} e^{-2\sigma_i^2 k^2} e^{-\frac{2R_i}{\lambda(k)}} \sin[2kR_i + \delta_i(k)] \quad (10)$$

The Debye-Waller factor corresponds to the degree of disorder due to both thermal vibrations and structural defects and S_0^2 is the passive electron reduction factor (about 0.8).

A sine function characterizes the oscillatory nature of $\chi(k)$ with a frequency proportional to the interatomic distance R. The amplitude (terms outside the sine) decreases with increasing wavenumber, k, so is in the denominator. The contribution of the shell atoms decreases with increasing distance from the absorber, which is accounted for in the first term as $1/R^2$ and in the third term as $\exp - 2R/\lambda(k)$. The photoelectron's mean distance—mean free path—that it travels, $\lambda(k)$, increases from 5 Å at $k = 2.5$ $Å^{-1}$ to 30 Å at $k = 15$ $Å^{-1}$. The scattering contributions within 10 Å dominate the EXAFS signal. Because it detects local structure, EXAFS is best for amorphous and crystalline macromolecules, solids, and liquids.

Because the contributions of all possible scattering paths overlap, the $\chi(k)$ spectrum is practically impossible to interpret quantitatively. However, converting $\chi(k)$

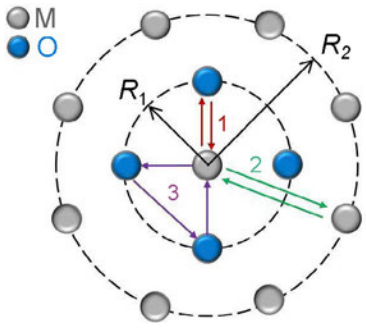

FIGURE 5 A central absorbing atom surrounded by two coordination shells of four atoms at distance R_1 and eight atoms at distance R_2. Besides the two direct scattering paths 1 and 2, multiple scattering paths such as 3 are possible. Adapted from Patience.[10] Copyright 2017 Elsevier

from the k domain to the R domain with a Fourier transform (FT), $\chi(R)$, facilitates data processing and interpretation:

$$\chi(R) = \int_{k_i}^{k_f} W(k) k^n \chi(k) [\cos(2\pi kR) + i\sin(2\pi kR)] \mathrm{d}k \quad (11)$$

where $W(k)$ is the window function (also called apodization) ($d_k = 1$) to dampen the extreme values of $\chi(k)$. $\chi(R)$ of Equation (11) comprises real (Re[$\chi(R)$]) and imaginary (Im[$\chi(R)$]) parts, which contribute to the magnitude of $\chi(R)$, affording an envelope of the real and imaginary parts:

$$|\chi(R)| = \sqrt{(\mathrm{Re}[\chi(R)])^2 + (\mathrm{Im}[\chi(R)])^2} \quad (12)$$

TABLE 1 Physical properties that account for the extended X-ray absorption fine structure (EXAFS) spectrum that include those that depend on the nature of the absorber and scattering atoms and structural parameters (Equation 10)

Property	Symbol	Dependency
Scattering amplitude	$F_i(k)$	Atoms
Phase shift	$\delta_i(k)$	Atoms
Photoelectron mean free path	$\lambda(k)$	Atoms
Average coordination number	N_i	Structure
Interatomic distance	R_i	Structure
Debye-Waller factor	σ_i^2	Structure

Each coordination shell is shifted about 0.25 Å towards shorter R because of the phase shift of each $\delta_i(k)$ parameter from Equation (10). Dedicated software that fits the spectrum determines the real interatomic distance as well as the coordination number and the Debye-Waller factor. Data processing to identify interatomic distances and coordination first normalizes the absorbance ($\mu[E]$), then extracts $\chi(E)$, converts the data from energy to wavenumber ($\chi(k)$), and finally transforms the spectra to the R domain (Figure 6).

The white line of the oxidized Pt(IV) in PtO_2 is more intense than the reduced metal Pt foil $\mu_{\beta PtO_2}(E) > \mu_{Pt}(E)$ (Figure 6A). The background subtraction extracts the oscillatory part above the adsorption edge (Figure 6B). The k^3-weighting magnifies the amplitude of the oscillations at higher energy (Figure 6C). Finally, FT of the EXAFS spectra clearly distinguishes the interatomic distances for Pt-O, Pt-Pt, Pt-Pt 1, and Pt-Pt 2 (Figure 6D).

The metal Pt foil $\mu(E)$ spectrum has a single intense peak at $R = 2.5$ Å. In fact, 12 Pt atoms in the first coordination shell surround Pt atoms in the cubic closest packed structure ($R = 2.774$ Å). βPtO_2 have at least three peaks in the $0 < R < 4$ Å range at 1.66, 2.85, and 3.28 Å. According to the βPtO_2 crystal structure (Figure 7), Pt is surrounded by four coordination shells within 4 Å: an octahedral coordination with 4 O atoms on the plane (Pt-O2 scattering path) at a distance of 2.023 Å and the two apical oxygen atoms (Pt-O1 path) at 1.916 Å, 2 Pt atoms at 3.138 Å (Pt-Pt1 path), and 8 (Pt-Pt2 path) at 3.555 Å.[15]

The overlap of the first two Pt-O1 and Pt-O2 shells in the $\mu(E)$ is too great to be resolved. On the other hand,

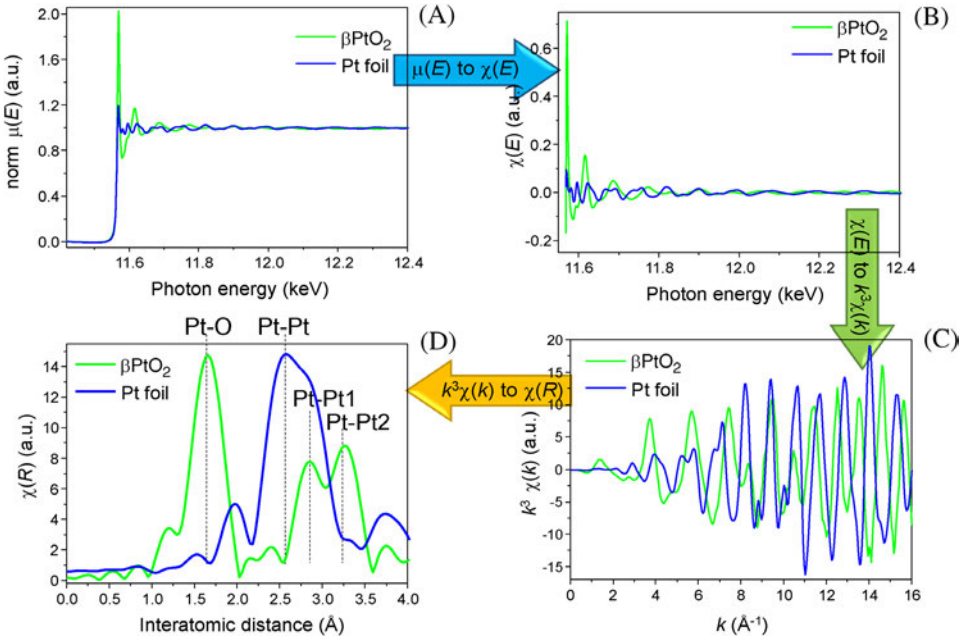

FIGURE 6 Extended X-ray absorption fine-structure (EXAFS) spectrum processing steps. Pt foil and βPtO_2 X-ray absorption spectroscopy (XAS) spectra at the Pt L3-edge energy (11 564 eV). (A) $\mu(E)$ normalized, (B) $\mu(E)$ EXAFS spectra after background extraction, (C) k^3 weighted $\chi(k)$ after transformation of the x-axis from energy to wavenumber, and (D) $\chi(R)$ Fourier transform EXAFS spectra. Adapted from Patience.[10] Copyright 2017 Elsevier

the Pt-Pt1 and Pt-Pt2 shells are sufficiently far enough away to analyze (Figure 6D), in the region above 2.5 Å, other multiple scattering paths only marginally contribute to the signal.

Resolving the local structure with EXAFS helps determine the likelihood of interactions of bimetallic compositions, for example. In-situ experiments demonstrate how stable materials are with respect to their environment—temperature, pressure, fluid composition, electromagnetic fields, or radiation. Furthermore, the average coordination number reveals information on nanoparticle size.

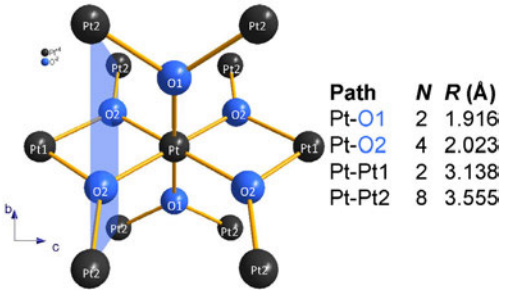

FIGURE 7 βPtO_2 crystal structure and Pt-O and Pt-Pt scattering shells. Adapted from Patience.[10] Copyright 2017 Elsevier

4 | APPLICATIONS

Over the last 12 years, the number of articles that mention XAS, XANES, EXAFS, or NEXAFS has plateaued at 1700 per annum. A bibliometric analysis grouped keywords into five clusters (Figure 8). The largest cluster (red in the map) focuses on electronic properties, optical properties, crystal structure, and includes other spectroscopic techniques like XRD,[6] XPS,[12] XAFS, NEXAFS, NMR (nuclear magnetic resonance),[23] and Raman.[24] The cluster with the second most number of keywords (green) contains oxidation, hydrogenation, Fischer–Tropsch, and metals—Cu, Ni, Co, Pt, Pd, and Au. The major keywords of the blue cluster are adsorption, speciation, mechanism, and reduction, and the compounds/elements include uranium (U—mostly U[VI]), Zn, phosphates, goethite, and ferrihydrite. The analytical technique Fourier transform infrared (FTIR) is assigned to the blue cluster, but is in the vicinity of the red cluster and is often applied together with the spectroscopic techniques of this

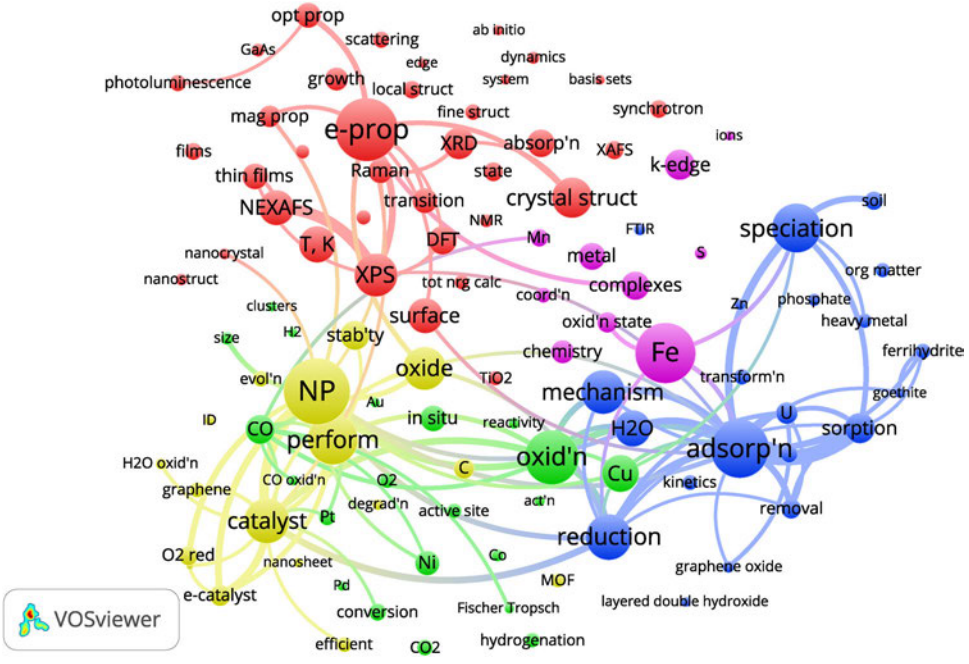

FIGURE 8 Bibliometric map of keywords from articles indexed by WoS from 2018 to September 2020 (4796 articles mention XAS, XANES, EXAFS, or NEXAFS).[21,22] The plot comprises 107 of the most often mentioned keywords that the VOSViewer software grouped together in five clusters (distinguished by their colour and the general close proximity): e-prop (electronic properties (37 keywords in the cluster), oxid'n (oxidation—21 keywords), adsorp'n (adsorption—21 keywords), NP (nanoparticles—17 keywords), and Fe (12 keywords). The size of the circles and fonts are proportional to the number of articles: e-prop (315 articles), oxid'n (273), adsorp'n (294), NP (333), and Fe (301). The smallest circles for each category are basis sets (49 articles), H_2 (47), layered double hydroxide (48), nanosheet (49), and ions (48). Lines represent citation links. The following keywords (and number of articles) were excluded from the map as they overlap too many other keywords as they are so large: XAS (1099), XANES (735), EXAFS (717), and spectroscopy (493)

cluster.[9] Nanoparticles (NP) dominate the yellow cluster, for which catalysis is the major theme including electrocatalysis (e-catalyst) oxygen reduction, water oxidation, carbon monoxide oxidation, stability, and metal organic frameworks (MOF). The magenta cluster, which bridges the blue and red clusters, concentrates on iron (Fe), metals, complexes, Mn, S, and K-edge.

Journal of Physical Chemistry C published 119 articles with XAS, XANES, EXAFS, or NEXAFS as keywords. The second most prolific journal was *Journal of Alloys and Compounds* (96 articles), followed by *Environmental Science & Technology* (94), then *Inorganic Chemistry* (92), *Physical Chemistry Chemical Physics* (92), and *ACS Catalysis* (86). The top five chemical engineering journals were *Applied Catalysis B-Environmental* (50), *Catalysis Today* (46), *Chemical Engineering Journal* (38), *Journal of Catalysis* (30), and *Fuel* (21). *The Canadian Journal of Chemical Engineering* (*Can. J. Chem. Eng.*) published articles that apply XAS and one dealing with catalysis (yellow and green clusters): 'CO_2 Conversion Through Combined Steam and CO_2 Reforming of Methane Reactions Over Ni and Co Catalysts,'[25] and the other with $LiFePO_4$ and batteries (red cluster) entitled 'Chemical Speciation and Mapping of the Si in Si Doped LFP Ingot with Synchrotron Radiation Technique'.[26,27]

Nature published the most cited article since 2018 entitled 'Reversible Mn^{2+}/Mn^{4+} Double Redox in Lithium-Excess Cathode Materials'.[28] Like the latter article in *Can. J. Chem. Eng.*, it concerns batteries and belongs to the red cluster. From April 2018 to September 2020, it accrued 171 citations. *Angewandte Chemie International* published the article 'Tailoring the *d*-Band Centers Enables Co_4N Nanosheets to be Highly Active for Hydrogen Evolution Catalysis',[29] which belongs to the yellow cluster as it deals predominantly with catalysis. The third most cited article was 'Nanoporous Copper Silver Alloys by Additive-Controlled Electrodeposition for the Selective Electroreduction of CO_2 to Ethylene and Ethanol' in *JACS*, which also belongs to the yellow cluster (catalysis).[30] The map shows that both XANES and EXAFS are used in catalysis to elucidate reaction mechanisms, structural studies of nanoparticles, MOF, TiO_2, and oxidation–reduction; thus, some examples will be presented herein.

4.1 | Vanadia–ceria catalyst for ethane ODH

XANES spectra are especially useful to determine oxidation state, electronic properties, local symmetry, and chemical environment of the absorbent element to understand the behaviour of catalytic materials. For example, vanadium systems are well known catalysts for partial oxidation reactions,[31,32] and adopt V^{III}, V^{IV}, and V^{V} oxidation states.[31,33] The Mars–van Krevelen mechanism characterizes how mobile oxygen from the lattice is incorporated to produce molecules.[34,35] Changing the vanadium/support interface affects the redox properties of the catalyst. XAS evaluates the vanadium oxidation state under reaction conditions, which establishes structure and reactivity relationships to better understand these systems and thus design more selective/active phases.

Here we consider vanadia–ceria systems and ternary $V_2O_5/CeO_2/SiO_2$ and the effect of silica support on new V-Ce-Si interfaces. Already, the literature has reported in-situ XANES spectra of vanadia–ceria redox cycles during ethane oxidative dehydrogenation (ODH).[36] The catalysts were prepared by impregnation of VOx on CeO_2/SiO_2 at 0.01, 0.03, and 0.03 gg^{-1} loading supports with 0.03 and 0.3 gg^{-1} CeO_2. Figure 9 shows the K-edge XANES spectra for the 5VCe, 1V3CeSi, 2V3CeSi, and 3V3CeSi. The spectra of all dehydrated samples (300°C in air) were essentially featureless, suggesting a similar local coordination and with a strong disorder at the local level. The absorption edge position is indicative of V^{5+} species in all cases. Under ODH reaction (red dashed line), different scenarios were observed for the V-Ce binary sample and for the V-Ce-Si ternary samples. In the case of 5VCe catalyst, the XANES spectrum shows

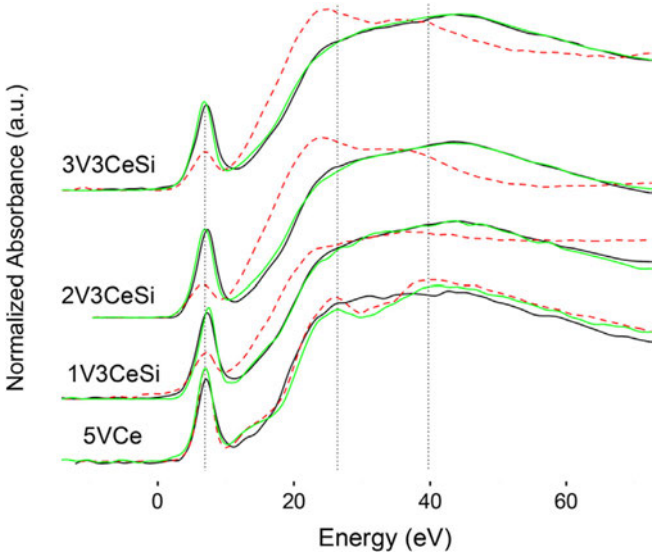

FIGURE 9 In situ V K-edge X-ray absorption near edge structure (XANES) of vanadium oxide molecularly dispersed on CeO_2/SiO_2. The support dehydrated in at 120°C for 16 h then calcined in air at 500°C for 16 h. Dehydration in air (black line): 300°C. ODH reaction conditions (red dashed line): $C_2H_6 + O_2 + He$ (ratio of 1:2:8) at 800°C. Oxidation conditions (green line): $O_2 + He$ mixture (ratio of 2:8) at 800°C. Adapted from Iglesias-Juez et al.[36] Copyright American Chemical Society 2018

the typical features of the $CeVO_4$ reference, demonstrating that ODH conditions promote the vanadate phase formation,[37,38] and therefore the V^{5+}/V^{4+} redox cycle is inhibited on the bare CeO_2 support. However, this was undetected on the CeO_2/SiO_2 support since both the shift of the spectra edge position and the decreasing pre-edge intensity are evidence of a reduced vanadium species. XANES data also show that this reduction process is reversible since the vanadium species oxidize to V^{5+} (green spectra) and reduce to V^{4+} under ODH conditions. A similar behaviour was also detected for a sample with a much higher content of CeO_2, 3V30CeSi (0.3 $gg^{-1}CeO_2$), indicating that the effect of silica on the structural reactivity of ceria also remains at high concentration of Ce in SiO_2, where bigger ceria entities are in contact with VOx centres.[36]

On the other hand, Ce L3-edge spectra have distinctive XANES features for Ce^{3+} and Ce^{4+} oxidation states and thus it is an appropriate technique to track its redox behaviour (Figure 10). In air (red), the 1V3CeSi XANES spectrum have two main peaks, B_2 and C, due to the excitation from the 2p core level into the bound 5d orbital and two shoulders (features labelled A and B1) that are only detected when Ce^{4+} is present, exactly like the pure CeO_2 reference.[39,40] The XANES spectrum changed completely under ODH conditions with the characteristic peak B_0 located at 5725 eV, distinctive of Ce^{3+} species, demonstrating that Ce centres become fully reduced (Figure 10-black). Later, when ethane was eliminated (oxidation), 1V3CeSi recovered the initial Ce^{4+} state, proving the Ce^{3+}/Ce^{4+} redox couple. However, as the V loading increased in the xV3CeV samples, it only partially reoxidized and the catalysts had a higher Ce^{3+} concentration, suggesting that vanadium is linked to the stabilization of the Ce^{3+} centres.

The mass fraction of Ce^{3+} was determined from the in-situ Ce L3-edge XANES spectra under ODH and air flow (Figure 11, left). The cerium oxidation state of the dehydrated xV3CeSi went from Ce^{4+} to Ce^{3+} under ODH reaction conditions. The oxidation state of the 3V30CeSi sample, with a higher Ce content, was higher, which suggests that vanadium promotes Ce^{3+} and only the centres at the interface with vanadium entities are susceptible to reduction (Figure 10). In all these samples, the ODH reduced V^{5+} vanadium species to V^{4+}. However, in the binary sample VCe, the Ce reduction was total, but a new Ce vanadate phase formed that blocked the redox couple of vanadium such that it remained in its initial V^{5+} state.

After, when air replaced the ethane, the degree of Ce reoxidation varied with V content: the higher the vanadium loading, the higher the % Ce^{3+} that remained oxidized (Figure 11, left, blue bars). This suggests that V species block the Ce^{3+}/Ce^{4+} redox couple. The $CeVO_4$ remained as Ce^{3+} as the O_2 environment was insufficient to reoxidize it. Raman spectroscopy, which is sensitive for V and Ce oxide species on SiO_2 support,[24,41] detected isolated surface V species near 1028 cm^{-1} This peak is attributable to the terminal V=O bond, that in the case of V-Ce samples was detected in the 1031 – 1036 cm^{-1}

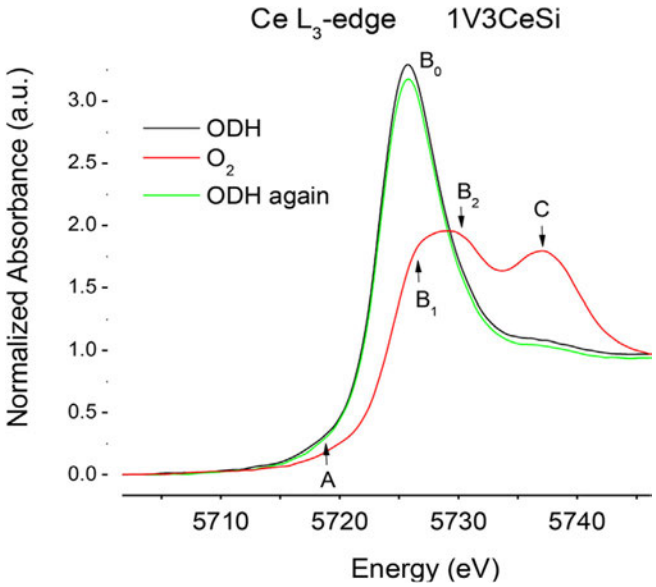

FIGURE 10 In situ Ce L_3-edge X-ray absorption near edge structure (XANES) spectra of 1V3CeSi at 800°C. Black line ODH mixture: $C_2H_6 + O_2 + He$ (ratio of 1:2:8). Red line oxidation: $O_2 +$ He (ratio of 2:8).Green line, second ODH exposure, $C_2H_6 + O_2 + He$ (ratio of 1:2:8). Adapted from Iglesias-Juez et al.[36] Copyright American Chemical Society 2018

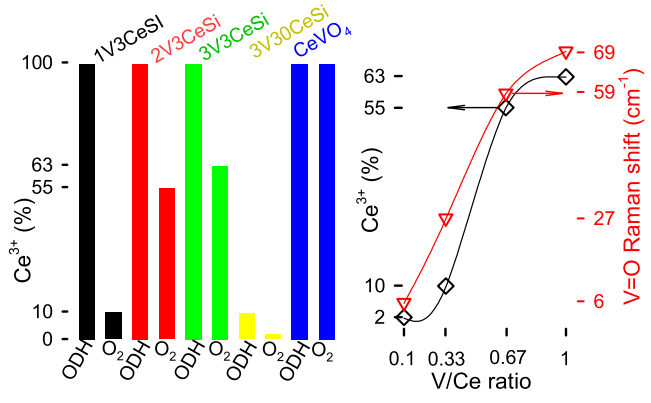

FIGURE 11 Degree of Ce reduction (% Ce^{3+}) calculated from in situ Ce L_3-edge X-ray absorption near edge structure (XANES) spectra of the samples under different conditions at 800°C: (grey) under ODH mixture, (blue) under air (C_2H_6 was removed from the mixture) (left). Degree of Ce reduction under air (blue square) versus V-to-Ce weight ratio and position of the V=O Raman mode in dehydrated used catalysts (orange triangle) (right). Adapted from Iglesias-Juez et al.[36] Copyright American Chemical Society 2018

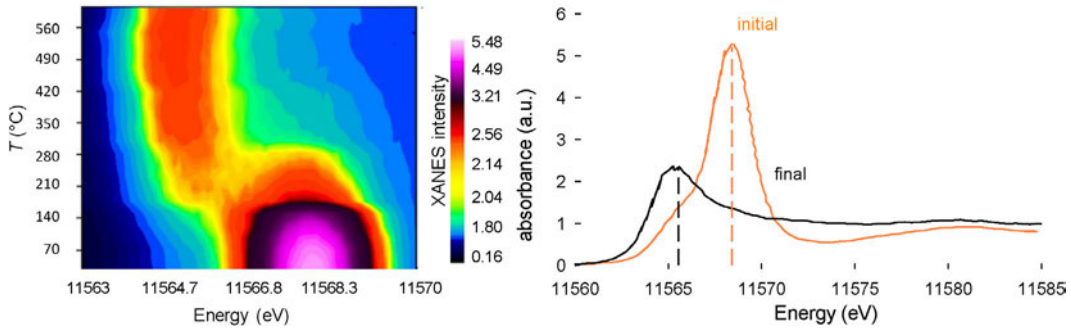

FIGURE 12 High energy resolution fluorescence detection X-ray absorption near edge structure (HERFD-XANES) spectra of Pt/Al_2O_3 catalyst measured during a temperature ramp to 600°C in H_2. Left panel: Intensity contour map. Right panel: Spectra of the initial and final Pt species formed. Adapted from Iglesias-Juez et al.[46] Copyright Elsevier 2010

range. This band shift suggests that dispersed VO species polymerize during reaction, especially with higher vanadium content, which would be related to the weaker interaction between V and Ce. The fraction of Ce^{3+} correlates with both the position of the V=O Raman of dehydrated used catalyst and V-to-Ce mass ratio (Figure 11, right). This example shows how in-situ XANES tracks oxidation state changes of species under reaction conditions and the importance of the relationship between support and active surface species. This example also demonstrates how the substrate affects the V-O-Ce interfacial chemistry.

Vanadium-based catalysts are dynamic species that change oxidation state when cycled between reducing and oxidizing atmospheres (Mars–van Krevelen redox couple).[42–44] In-situ XANES is one spectroscopic technique to study the active phases in each environment to determine the reaction mechanism and design a better catalyst.

4.2 | Pt-Sn for propane dehydrogenation

Pt-based catalysts dehydrogenate propane to propylene. Propylene demand is growing rapidly with the propane supply in the US due to shale gas production.[45] Sn, as a promoter, modifies the catalytic behaviour of Pt. High energy resolution fluorescence detection (HERFD)-XANES during H_2 reduction and consecutive dehydrogenation-regeneration cycles is capable of quantifying Pt reducibility, particle size, and the extent of Pt-Sn alloying.[44] Pt is oxidized prior to feeding hydrogen and the edge shifts to lower energies with a corresponding drop in the white-line intensity during hydrogen treatment, which confirms Pt reduces to metallic Pt around 140–210°C (Figure 12). Similarly for Pt-Sn catalyst (Figure 13), the Pt species reduce to Pt, but above 210°C a Pt-Sn alloy forms.

Heating to 600°C in propane induced changes detectable by HERFD-XANES for both Pt and Pt-Sn samples.[46] $\Delta\mu$ difference spectra were calculated using bare metal at the same temperature as a reference to substantiate these changes (Figure 14a):[47,48] A negative feature near 11 564 eV and a positive peak near 11 567 eV are evident in the spectrum and both signals reach a maximum at 140°C, indicating changes in the electronic structure due to propane adsorption (Figure 14, left panel). The negative signal corresponds to an edge shift to higher energies, and the positive to increased white-line intensity that broadens on the high-energy side. Based on previous XAS studies on Pt surface with CO and ethane adsorption,[48,49] a reduction in electron density from the Pt cluster to the adsorbate, accounted for the increase in the white-line intensity and edge position shift to higher energies. Thus, the two peaks are attributable to propene species and/or adsorbed H_2 on the Pt clusters (both of which form during the reaction). In the case of the Pt-Sn sample (Figure 14, right panel), the spectra have only one positive peak, which indicates that hydrogen adsorption is negligible.[50] For Pt-Sn, the shift of the edge position to lower energies indicates that electrons transfer from the adsorbate to the metal; a Pt-propylene complex forming σ-bond accounts for this feature. Since Sn removes the charge form Pt, a π-bond does not form, which confirms that the Pt-Sn interaction weakens the surface chemisorption. This implies that the selective C-H bond activation is favoured with respect to $C\text{-}C^-$ or C=C, increasing the selectivity to propylene. In addition, coke precursors (hydrocarbons) desorb more easily from the Pt-Sn surface compared to Pt, which explains the higher selectivity and stability of Sn promotion.

In this same study, the structural evolution of the alloy was measured during successive reaction-regeneration-activation cycles (as in industrial operations), confirming the progressive increase in particle size and Sn enrichment

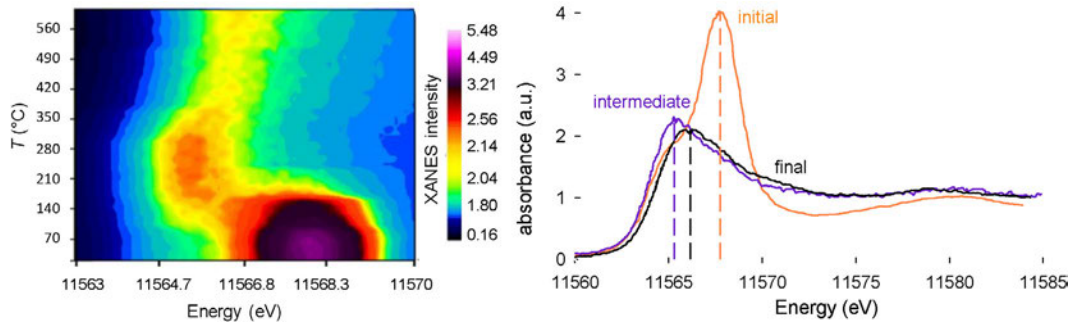

FIGURE 13 High energy resolution fluorescence detection X-ray absorption near edge structure (HERFD-XANES) spectra of Pt-Sn/Al_2O_3 catalyst measured during a temperature ramp to 600°C in H_2. Left panel: Intensity contour map. Right panel: Spectra of the initial and final Pt species formed. Adapted from Iglesias-Juez et al.[46] Copyright Elsevier 2010

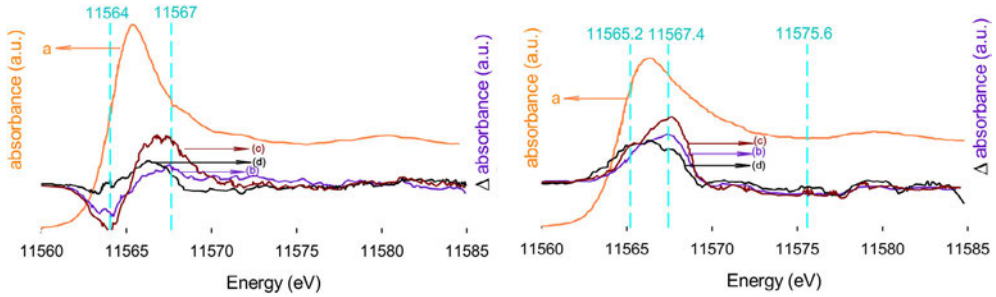

FIGURE 14 L_3-edge $\Delta\mu$ difference X-ray absorption near edge structure (XANES) spectra during a temperature ramp in propane. Left panel: (a) Pt/Al_2O_3 reference (b) 100°C, (c) 122°C, and (d) 400°C. Right panel: (a) Pt-Sn/Al_2O_3 (b) 100°C, (c) 140°C, and (d) 400°C. Adapted from Iglesias-Juez et al.[46] Copyright Elsevier 2010

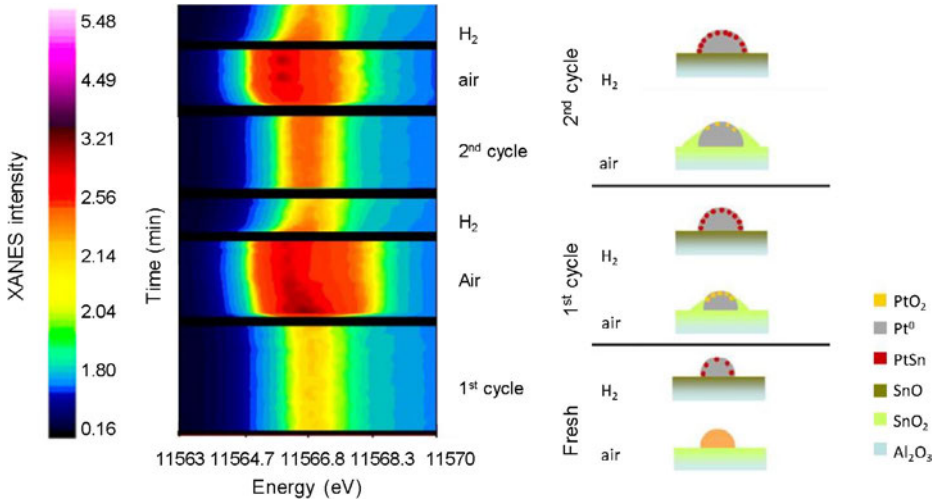

FIGURE 15 High energy resolution fluorescence detection X-ray absorption near edge structure (HERFD XANES) spectra of Pt-Sn/Al_2O_3. Left panel: Intensity contour map during the first two propane dehydrogenation-regeneration cycles at 600°C. Right panel: Model of the Pt and PtSn species before and after successive air and H_2 treatments. Adapted from Iglesias-Juez et al.[46] Copyright Elsevier 2010

of the alloy, which supports the rationale of the observed deactivation after successive cycles (Figure 15).

This *operando* XAS study determined morphological and structural information and how the electronic properties of the Pt-centres depend on the Sn alloy degree, which changes as a function of oxidation and reduction treatment. These results suggest that these differences modify the activation of the hydrocarbon and alter the nature and strength of the adsorption of reactants and products.[46]

4.3 | PdZn over ZnO for 1,3-butadiene hydrogenation

Combining XAS (a predominantly bulk technique) with surface sensitive spectroscopic techniques like Raman[9] or IR[24] increases the capability of relating reaction rates and structure. In this example, XAS was combined with DRIFTS to study 1,3-butadiene hydrogenation. The spectra confirmed that the stability of the adsorbed intermediates depended on the ZnO nanoparticle shape with

distinct planar surfaces and degree of alloying. The alloys' electronic and structural properties determined the hydrogenation selectivity.[51] The nature of the exposed face of the ZnO support modulates the interaction between Zn and the active phase, which determines what type of PdZn alloy forms. These experiments required a specially designed cell to measure XAS and DRIFTS (diffuse reflectance infrared Fourier transform spectroscopy) simultaneously while a mass spectrometer monitored the effluent gas composition.[51] The formation of PdZn alloys was investigated by in-situ XANES during H_2-temperature programmed reduction (TPR) (Figure 16) on TiO_2 (as a reference for non-alloyed Pd), ZnO-n needles, ZnO-b bricks, and ZnO-t tetrapods supports. Based on the XRD and high-resolution transmission electron microscopy (HRTEM) measurements, the Pd-ZnO-n maximizes the exposure of the polar planes, while in the Pd-ZnO-t the proportion of nonpolar (1010) planes were maximized, and for Pd-ZnO-b it was the nonpolar (1120) surface.[51] The XANES spectra for all samples (Figure 16) are typical of Pd(0) species, but there are some differences in the shape compared to a Pd foil depending on the support, suggesting that the electronic density of Pd on the ZnO supports was higher compared to the Pd foil.[52] We infer this by comparing the energy position of both the edge (expanded view), and the CRs (continuous resonance shapes), and their intensity, of the ZnO spectra with the $Pd-TiO_2$ and foil.

These effects indicate that Zn atoms transfer electronic density to empty Pd states by alloy formation. Particle size accounts for differences between the supported ZnO samples.[53] Zn diffusion into the Pd structure increases Pd-Pd distances and decreases the CRs position ($1/R^2$ rule), which explains the energy shift of CRs. These

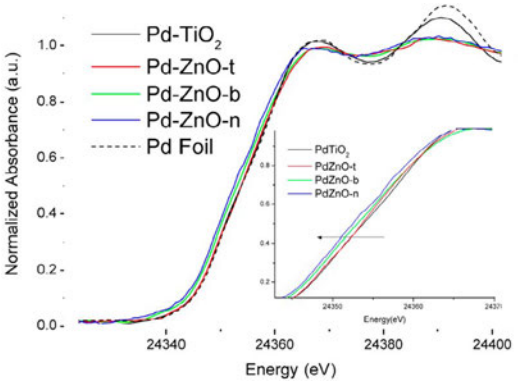

FIGURE 16 Pd K-edge X-ray absorption near edge structure (XANES) spectra for the final species after temperature programmed reduction (TPR) in H_2 for Pd-TiO_2, PdZnO-t, Pd-ZnO-b, Pd-ZnO-n, and Pd foil reference. Adapted from Castillejos-López et al.[51] Copyright American Chemical Society 2017

data suggest a PdZn alloys form. In the case of $Pd-TiO_2$, the Pd reduces just after H_2 contact and it forms the largest Pd particles, stabilizing as a hydride phase when the temperature is decreased.[51] On the contrary, when Pd is supported on ZnO, the interaction of Pd species with Zn delays the reduction of Pd species to higher temperatures, pointing to different redox properties, which is expected to affect the catalytic behaviour of these materials. These interactions depend on the specific plane where the Pd species attach: The alloy forms at higher temperature for the stronger interactions. The weakest interaction (and lowest onset formation temperature) is for Pd-ZnO-n, followed by Pd-ZnO-b, and finally Pd-ZnO-t.

The Pd-Pd atomic distance in the first coordination shell is 2.80 Å for $Pd-TiO_2$, higher than the characteristic value for metallic Pd foil or reference at 2.750 Å (Figure 17, Table 2). This difference indicates that H atoms diffuse into the FCC Pd structure (faced-centred cubic) to form a hydride nanoparticle phase.[54,55] In the case of ZnO supported samples, the atomic distances are even greater (Table 2). Introducing an additional Pd-Zn coordination shell with smaller distances fit the spectra best, which confirms that an alloy forms. The Pd-Zn coordination number increases from 0.6 to 1.4 (Table 2), which suggests that the Zn content is highest in the Pd-ZnO-n alloy. Comparing the coordination number of Pd-Pd and Pd-Zn shells, the Zn content of the Pd-Zn alloy lies between $0.14-0.20\ gg^{-1}$.[51] However, at higher temperature, the EXAFS analysis indicates that a 1:1 PdZn alloy forms. The electron density and elongation of the lattice of the Pd-Pd bonds increases with Zn content.

The shape of the XANES spectra was substantially the same while cycling between H_2 + 1,3-butadiene and H_2 atmospheres, which confirms that the Pd-Zn structure is stable under reaction conditions.[51] DRIFTS spectra showed that 1,3 butadiene was adsorbed in all the samples after 10 min along with some reaction products; for pure Pd, n-butane was detected, but for the PdZn alloy, 1- and 2-butenes IR fingerprints were present. The DRIFTS bands assert that the PdZn alloy changes the adsorption capacity of the reaction products: On pure Pd, the adsorption is fast and products saturate the surface more quickly. On the contrary, product adsorption is slower on the alloy. The distinct catalytic behaviour of the ZnO-supported catalysts in comparison with the $Pd-TiO_2$ catalyst can be explained by both the electron-rich Pd active sites and isolated active Pd atoms. These effects account for the distinct catalytic behaviour of the ZnO-supported catalysts in which a PdZn intermetallic alloy forms after H_2 reduction. This study demonstrated the potential of XAS to identify the local structure of active sites and its relationships with their reactivity.[51] The potential of XAS is reinforced when combined with

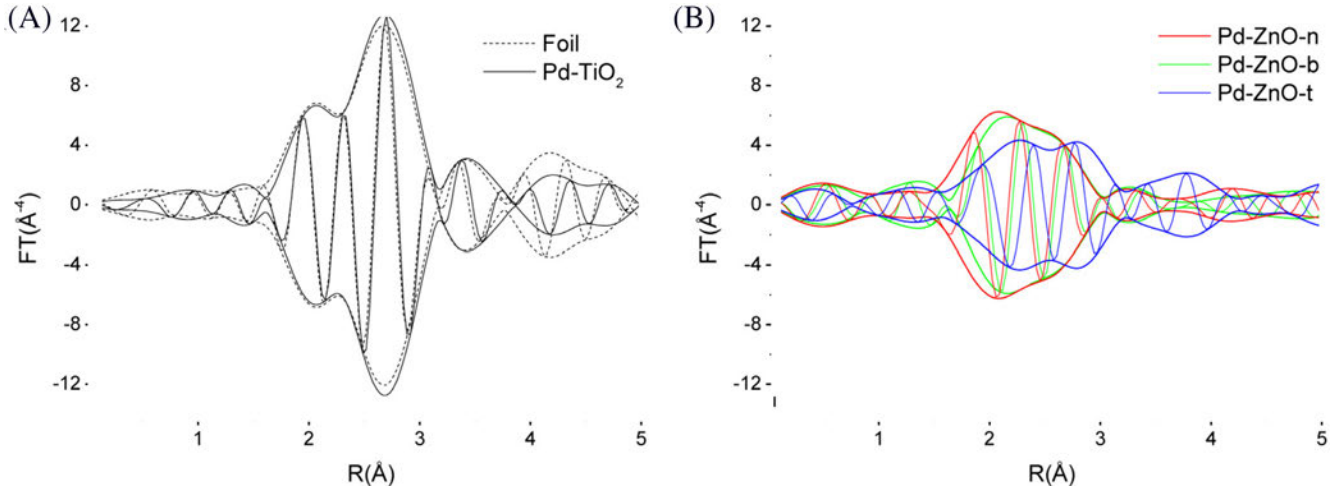

FIGURE 17 k^3-weighted modulus and imaginary part of the Fourier transform of Pd K-edge extended X-ray absorption fine structure (EXAFS) spectra corresponding to the reduced catalyst at room temperature: (A) Pd – TiO_2 and (B) Pd on ZnO supports. The Fourier transform of the Pd foil is shown using dotted lines as reference. Adapted from Castillejos-López et al.[51] Copyright American Chemical Society 2017

TABLE 2 Pd catalysts structural parameters from ambient temperature after reduction up to 250°C (Figure 17)[51]

	Pd-Zn shell		Pd-Pd shell		
Sample	R	N_1	R	N_2	N_1/N_2
Pd-TiO_2			2.80	8.5	
Pd-ZnO-t	2.54	0.6	2.90	2.1	0.3
Pd-ZnO-b	2.49	1.3	2.86	1.5	0.9
Pd-ZnO-n	2.51	1.4	2.88	1.4	1

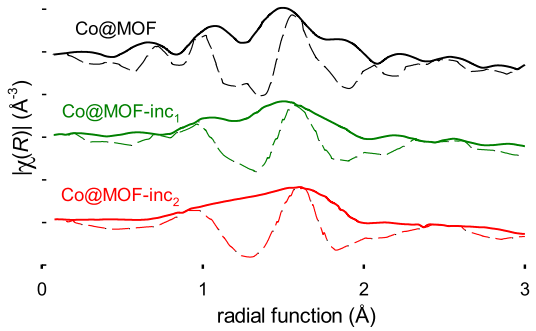

FIGURE 18 k^2-Weighted modulus and real part of the Fourier transform of Co k-edge extended X-ray absorption fine structure (EXAFS) spectra corresponding to Co@MOF before (black) and after incubation periods: (green) $inc_1 = 12$ h and (red) $inc_2 = 24$ h. Adapted from Iglesias-Juez et al.[56] Copyright Royal Society of Chemistry 2018

complementary IR spectroscopy that adds relevant chemical information to the electronic and structural insights obtained by XAS. The simultaneous acquisition also guarantees identical experimental conditions (T, P, gas composition...), ensuring comparable results.

4.4 | Photocatalytic H_2 production

XAS coupled with electron paramagnetic resonance (EPR) to optimize Co-based photocatalyst composition for H_2 production is another example of the power of combining spectroscopic techniques.[56,57] Like the previous example, specially designed liquid–solid–gas reactors are required to measure species composition in situ. In this case, *operando* XAS monitored the catalysts during a pre-reaction (incubation) period as well as during photocatalytic hydrogen production to examine the structural and electronic behaviour of the photocatalysts (Figure 18). The EXAFS spectra FT of Co-K-edge of Co@MOF catalyst before and after incubation period indicate that Co^{2+} species initially have an octahedral first coordination sphere with O and/or N atoms, and with Br to a minor extent. One limitation of EXAFS is the difficulty in distinguishing O and N, since they have similar atomic numbers and are light scatterers. However, previous IR analysis confirm that N is part of the lattice.[58] The EXAFS fitting results (Table 3) indicate that the Co-N distance increases during incubation, with a decrease in Co–Co coordination number, and with the absence of a second coordination Co–Co shell, since the coordination number is below 0.3. The shape of EXAFS spectra (Figure 18) indicate that there are several differences between the fresh and the incubated sample, that could be related to the presence of a cobalt-MOF wall interface contribution. Thus, it was necessary to introduce another Co-Ti coordination shell to better fit the data, suggesting that Co monomers were stabilized by bonding to the Ti oxo-cluster of the MOF. Fitting results (distances and coordination numbers) coupled to EPR data suggest Co bonds to Ti-clusters through oxo-bridges.

This interaction with Ti is crucial for catalytic activity since Co^{2+} species encapsulated on other Zr- or Al-based MOFs supports following the same synthesis methods formed catalytically inactive phases.[59]

The mechanism and how visible light induced the catalytic activity were explained by *operando* XANES experiments under reaction conditions. Here, differential methods were applied to enlarge spectra changes. Figure 18 presents the intensity colour maps of the normalized differential XANES spectra obtained while switching the light on and off.[58] The light shifts the edge to lower energy, a corresponding drop in white line intensity, and a shoulder near 7737 eV. This is related to the increase in electron density of the p and d states, indicative of a partial reduction of the cobalt sites. After 5 h, steady state was reached coinciding with the beginning of the reaction. All these changes were reverted once the light was switched off. This behaviour was reproducible during the second light exposure cycle (Figure 18). Therefore, the study highlights what happens during the incubation stage: initial Co-diners partially dissociate and monomer Co(II) species connect to Ti-clusters through oxo-bridges. Light excites Ti-oxoclusters in the structure and the electron density accumulates in the Co-sites, electronically coupled to the Ti atoms of the MOF material. These partially reduced cobalt sites are the active catalytic centres that produce H_2.

4.5 | Photocatalytic CO_2 photoreduction

A similar experimental procedure was applied to study photocatalysis with Ag nanoparticles supported on TiO_2 to reduce CO_2.[60] The *operando* XANES study (Figure 19) identified how charge transferred in UV and visible light: UV light promotes electrons from the titania valence band to the conduction band (3d states of Ti) and then to Ag. The charge accumulated in the Ag-centres reduce the CO_2 to CH_4. Under visible light, Ag 5s orbitals donated electrons to the 2p orbitals of oxygen neighbour atoms and the 3d of Ti, This charge transfer coincided with the formation of intraband-gap interface states from strong dielectric coupling at the interface between plasmonic Ag nanoparticles and TiO_2.

5 | UNCERTAINTIES

5.1 | Limitations

XAS effectively analyzes the chemistry of dynamically changing systems under reaction conditions, but it requires a synchrotron. Furthermore, it requires the design of cells or complex setups and specialists to analyze the spectra.[61] Several in-situ cells have been designed enabling experiments to be performed at high or low temperature; under vacuum or high pressure; and under flowing inert, reducing/oxidizing, or reactive atmosphere.[61–65] In-situ cells have also been designed for gas sensors investigation[66] or as autoclaves for XAS studies in high temperature fluids ($< 400\,^{\circ}C$).[67] Their specific character due to the quantification of the absorption levels allows a specific element within a matrix to be studied. However, spectra of samples that are thicker than the X-ray penetration depth or diluted in a matrix of heavy, highly absorbing elements have low signal-to-noise ratios because of the low intensity of transmitted X-rays. This is common in heterogeneous catalysts such as noble metals deposited in low amounts on a support of heavy elements (e.g., $0.02\ gg^{-1}$ Pd supported on $Ce_{1-x}Zr_xO_2$[68] or $0.005\ gg^{-1}$ $Pd/LaCoO_3$) or thin films deposited on thick support.[69,70] Recording spectra in the fluorescence mode improves the signal strength.

XANES requires reference systems that have similar crystallinity (particle size). EXAFS analysis requires amplitude functions and phase shifting from experimental references or theoretical calculations. On the other hand, the extreme spatial localization of the initial state, a core level, infers a local character to XAS. XAS is sensitive to the order present in the material from atomicity up to approximately 15 Å. XANES has an inherent high signal-to-noise ratio as it is unaffected by thermal effects, which allows in-situ studies. The signal-to-noise ratio of the EXAFS spectra is usually low, which compromises the interpretation of the signal. The technique is sensitive to thermal (vibrational) effects and, therefore, requires low temperature spectra for closed (analytical) formulas. Finally, the recent trend in beamline instrumental development involves combining several

TABLE 3 Co catalyst structural parameters derived from extended X-ray absorption fine structure (EXAFS) (Figure 18); numbers in parentheses are the errors in the last digit[56]

Coord.	Fresh		Incubated$_2$	
Shell	***N***	***R* (Å)**	***N***	***R* (Å)**
Co-O	5.9(9)	2.14(4)	3.8(2)	2.05(2)
Co-N	-	-	1.5(3)	1.93(1)
Co-Br	0.5(3)	2.45(3)	-	-
Co-Co	0.8(4)	3.39(5)	0.2(2)	2.84(3)
Co-Ti	-	-	0.8(2)	3.08(2)

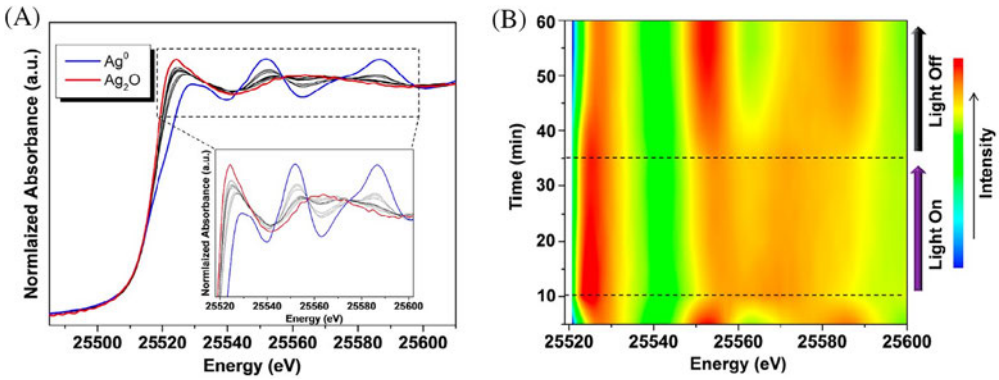

FIGURE 19 Ag K-edge X-ray absorption near edge structure (XANES) spectra during (A) exposure to the X-ray beam and during UV light switching under reaction conditions (B) during a cycle of successive on/off external blue illumination. Reproduced from Reñones et al.[60] Copyright American Chemical Society 2020

complementary spectroscopic techniques in a single experiment, such as XAFS+XRD,[71,72] XAFS +DRIFT,[61,73] and XAFS+Raman.[72]

5.2 | Surface sensitivity

All the described methods have the limitation of reporting the average state of the element, which makes XAS a bulk technique. In the last decades, several studies have addressed XAS surface sensitivity to probe the reactivity of surface species in heterogeneous catalysts.[74] Studying material surfaces under dynamic conditions, like adsorption/desorption of a probe molecule or redox dynamics, provokes only subtle variation in the XAS spectrum. A first attempt to extrapolate this subtle variation from the spectrum is the $\Delta\mu$ XANES technique.[47,75,76] This technique has been applied to estimate the CO/Pt coverage during the CO oxidation on a Pt electrode.[77] The $\Delta\mu$ spectrum is the difference between the experimental spectrum (e.g., after CO adsorption on Pt) and a reference spectrum (e.g., pristine Pt). The reference spectrum is then compared with a simulated one to identify adsorbed specie and coverage. The main problem of this approach is that the obtained difference spectrum is noisy and requires a post smoothing manipulation. A possible alternative is the modulated excitation XAS (MEXAS) technique.[73,78,79] MEXAS is achieved through the cyclic variation of the experimental conditions (e.g., gas composition or concentration, pressure, pH, potential, irradiation),[80] while recording time resolved XAS spectra. The cycles are then merged in order to obtain a single set of averaged time resolved spectra with an improved signal-to-noise ratio. This applies fully reversible processes (such as catalytic reactions) and for well-synchronized spectra measurements. Finally, MEXAS exploits the phase sensitive detection (PSD) algorithm to extract the response of the active species by filtering the signals of spectator species (including the background) and the noise.[80,81] Hence, the obtained demodulated spectra are formally similar to difference spectra but with a significantly improved signal-to-noise ratio.

5.3 | Detection limits, quantitative analyses, and wavelet transform

XAS quantifies the oxidation state of the bulk. Complementary techniques such as IR, XPS,[82,83] or Raman[24] are necessary to quantify the percentage of a specific oxidation state on the surface. In EXAFS, it is impossible to distinguish between scattering atoms with little difference in atomic number: C, N, O or S, Cl, or Mn and Fe, for example. Indeed, XAS usually identifies the nature of the neighbouring atoms according to their distances from the central atom after a Fourier transform. The FT-EXAFS spectrum becomes harder to interpret because of the limited available k range, which broadens the peak to the same order of magnitude of the FT spectrum. A k data range for FT of at least $2-12$ Å^{-1} is appropriate. Spectra of bulk materials usually extend the k range even up to $2-16$ Å^{-1}. The spatial resolution in R increases with an increase in k range because of the narrowing of the FT peak. In general, a spatial resolution of 0.15 Å^{-1} is possible. Moreover, if a coordination shell comprises different elements of similar atomic radius, they cannot be resolved by the FT approach because they are all placed at similar interatomic distance. Usually this problem is solved by trial-and-error fits. A more sophisticated and useful approach is the wavelet transform of the EXAFS spectrum.[84–86] The wavelet transform produces a $R(\text{Å})$ versus $k\left(\text{Å}^{-1}\right)$ 2D contour map to help visualize and discriminate elements within one atomic shell.[87] This high spatial resolution facilitates generating XANES spectra in multiple areas or zones of sample that have been applied in catalysis to identify the distribution and composition of active species and/or spectators under reaction conditions. With this approach (*operando* space-resolution EXAFS analysis), Dann et al.[88] studied how

the ignition of CO oxidation reactions coincide with the oxidation of Pd nanoparticles on catalyst surfaces, confirming the Langmuir-Hinshelwood reaction mechanism. Beale and coworkers[89] produced 3D images of a carbon-supported Mo-Pt industrial catalyst with scanning XANES tomography to visualize the distribution of both Pt (active) and Mo (promoter) phases. The results showed how Pt species tend to concentrate on the surface of the carbon support, especially in the internal pore structure. The results also suggested that the catalytic activity is enhanced when Pt and Mo are in close proximity.

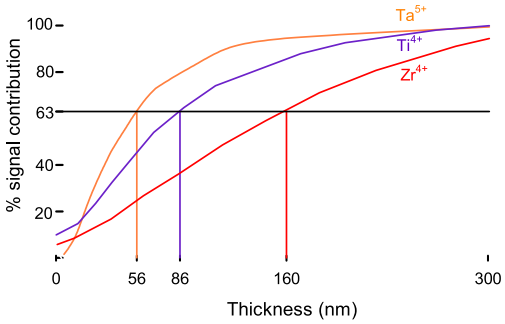

FIGURE 20 Oxide contribution to extended X-ray absorption fine structure (EXAFS) spectra as a function of film thickness. Adapted from Jiménez et al.[99]

5.4 | Sources of error

The raw XAS spectrum is obtained from a plot of the $\ln(I_0/I)$ versus E (Figure 3). XAS spectra must be normalized to remove sample concentration and density and thickness dependency of the edge jump intensity, and to allow quantitative analysis and comparison between spectra of different materials and experiments independently of the experimental conditions, chemical composition, and concentration.

Higher flux synchrotron sources improve signal-to-noise ratio but at the same time generate beam damage problems and heating effects faster, which is a major drawback. This problem is becoming more prevalent with the advent of these brilliant X-ray sources. The latest generation of X-ray facilities with improved detector efficiencies reduce measurement times with a good signal-to-noise ratio even in the case of very diluted systems, but at the cost of delivering much higher photon doses than older synchrotrons.

The interaction of the radiation with the sample or its environment could modify atomic structure, crystal structure, or chemical state but also other parameters such as sample temperature and sample environment (gases, liquids). This may affect the interpretation of the results; thus, the acquisition time must be minimized. Another option is to move the sample during the analysis, in order to reduce the energy dosed per unit surface of the sample.[90] The strategy depends on if the sample is liquid or solid. With liquid samples, large acquisition times are used while the sample recirculates to avoid sample overheating. In the case of solid samples, the time acquisition must be as short as possible, and in different points of the sample, in order to avoid sample damage. In all cases, the working temperature should be minimized. In the case of solid samples the heterogeneity of the particle size can also give artefacts in the XANES spectra.[91] The structural damage or oxidation state changes following X-ray exposure should be recognized and quantified to be able to correctly interpret experimental results. The issue becomes especially relevant when dealing with non-invasive monitoring of small and/or delicate samples,[92] accurate analysis of surfaces,[93] and investigation of biological diluted samples.[94] Examples of the latter are proteins in complexes with transition metal ions,[95] as their oxidation state can change under radiation,[96] and because of chemical reactions with naturally abundant reducing agents.[97,98]

5.5 | Penetration depth

Jiménez et al.[99] assessed XAS penetration depth for TiO_2, Ta_2O_5, and ZrO_2 based on the total electron yield. They prepared oxide samples with different thicknesses supported on the metal. Firstly, they analyzed the intensity of the edge peak of each element when going from pure metal to a thick layer of the metal oxide to show how the spectra is composed of two components that correspond to the metal and to the oxide. Then, they plotted the percentage of oxide detected in the different oxide/metal samples as a function of the oxide thickness. The percentage of the oxide signal contributing to the EXAFS spectra approached 100% after 200 nm for TiO_2 and Ta_2O_5 but only reached 90% for ZrO_2 at 200 nm (Figure 20). The thickness of the oxide layer for each at a 63% contribution was 56, 86, and 160 nm for Ta_2O_5, TiO_2, and ZrO_2, respectively. The energy of the analyzed edge and the density of the materials were found to be the main factors that determine the information depth. Film heterogeneity contributes to the uncertainty in identifying contribution to the EXAFS spectra from surface species, like thin films, and support. This series of tests demonstrated the influence of the edge energy on the penetration depth, the density of the targets, and the possible differences between the energies of the Auger electrons generated by photoionization of K and L edges.

6 | CONCLUSIONS

XAS is a powerful technique to identify the local atomic structure around the absorbing atom as well as its oxidation state. We included examples of XANES and EXAFS spectra for nanoparticle active centres, both metallic and oxides, systems supported on an oxide material, and those encapsulated inside the pores of a MOF. These catalytic sites are virtually impossible to characterize with conventional techniques due to their low mass fraction and particle size. The gas–solid phase and liquid–solid phase systems, representative of both thermal and photochemical catalysis, further illustrate the breadth of the possible applications. XAS discloses catalytic phenomena related to electronic, geometric, and surface properties. When combined with surface sensitive spectroscopy (Raman, FTIR, EPR/ESR) in *operando*, XAS is capable of identifying structure–activity relationships to better design more efficient and sustainable catalyst systems and processes. Current research trends include bench scale light sources to characterize hazardous materials and examine catalytic stability and surface sensitive techniques (MEXAS) to identify adsorbed species and coverage.

ACKNOWLEDGEMENTS

The authors acknowledge travel support from the Erasmus+ KA107 (2018-1-ES01-KA107-049563) and funding for the open access charge from the Universidad de Málaga/CBUA. This work was undertaken, in part, thanks to funding from the Canada Research Chairs program (950-231476).

PEER REVIEW

The peer review history for this article is available at https://publons.com/publon/10.1002/cjce.24291.

ORCID

Gian Luca Chiarello https://orcid.org/0000-0003-4550-175X
Gregory S. Patience https://orcid.org/0000-0001-6593-7986
M. Olga Guerrero-Pérez https://orcid.org/0000-0002-3786-5839

REFERENCES

[1] W. Röntgen, *Sitzungsberichte der Physikalish-Medizinischen Gesellschaft zu Würzburg* **1895**, *137*, 132.
[2] R. W. Johnston, D. H. Tomboulian, *Phys. Rev.* **1954**, *94*, 1585.
[3] F. W. Lytle, *J. Synchrotron Radiat.* **1999**, *6*, 123.
[4] A. Mottana, A. Marcelli, in *A Bridge Between Conceptual Frameworks*, History of Mechanism and Machine Science, Vol. 27 (Ed: R. Pisano), Springer, London, UK **2015**, p. 275.
[5] G. S. Patience, C. A. Patience, F. Bertrand, *Can. J. Chem. Eng.* **2018**, *96*, 1684.
[6] H. Khan, A. S. Yerramilli, A. D'Oliveira, T. L. Alford, D. C. Boffito, G. S. Patience, *Can. J. Chem. Eng.* **2020**, *98*, 1255.
[7] G. S. Patience, *Can. J. Chem. Eng.* **2018**, *96*, 2312.
[8] F. S. Rocha, A. J. Gomes, C. N. Lunardi, S. Kaliaguine, G. S. Patience, *Can. J. Chem. Eng.* **2018**, *96*, 2512.
[9] M. O. Guerrero-Pérez, G. S. Patience, *Can. J. Chem. Eng.* **2020**, *98*, 25.
[10] G. S. Patience, *Experimental Methods and Instrumentation for Chemical Engineers*, 2nd ed., Elsevier B.V, Amsterdam, The Netherlands **2017**.
[11] A. Das, N. Yadav, S. Manchala, M. Bungla, A. K. Ganguli, *ACS Omega* **2021**, *6*, 1007.
[12] J. P. Holgado, A. Caballero, J. Espinós, J. Morales, V. M. Jiménez, A. Justo, A. R. González-Elipe, *Thin Solid Films* **2000**, *377–378*, 460.
[13] P. Zimmermann, S. Peredkov, P. M. Abdala, S. DeBeer, M. Tromp, C. Müller, J. A. van Bokhoven, *Coordin. Chem. Rev.* **2020**, *423*, 213466.
[14] G. Margaritondo, *Elements of Synchrotron Light*, Oxford University Press, Oxford, UK **2002**.
[15] D. C. Boffito, C. Neagoe, G. Cerrato, C. Boffito, G. L. Chiarello, C. L. Bianchi, M. G. Rigamonti, A. Benamer, G. S. Patience, in *Experimental Methods and Instrumentation for Chemical Engineers*, 2nd ed. (Ed: G. S. Patience), Elsevier B.V, Amsterdam, The Netherlands **2017**, p. 339.
[16] B.-K. Teo, P. A. Lee, *J. Am. Chem. Soc.* **1979**, *101*, 2815.
[17] S. Yamazoe, Y. Hitomi, T. Shishido, T. Tanaka, *J. Phys. Chem. C* **2008**, *112*, 6869.
[18] J. J. Rehr, J. J. Kas, F. D. Vila, M. P. Prange, K. Jorissen, *Phys. Chem. Chem. Phys.* **2010**, *12*, 5503.
[19] H. Al-Mahayni, X. Wang, J.-P. Harvey, G. S. Patience, A. Seifitokaldani, *Can. J. Chem. Eng.* **2021**, *99*, 1885.
[20] The FDMNES project 2020, http://fdmnes.neel.cnrs.fr (accessed: May 2020).
[21] N. J. van Eck, L. Waltman, *Scientometrics* **2010**, *84*, 523.
[22] Web of ScienceTM Core Collection 2020, http://apps.webofknowledge.com (accessed: July 2020).
[23] M. G. Rigamonti, F. G. Gatti, G. S. Patience, *Can. J. Chem. Eng.* **2019**, *97*, 628.
[24] M. O. Guerrero-Pérez, G. S. Patience, *Can. J. Chem. Eng.* **2020**, *98*, 25.
[25] M. Shakouri, Y. Hu, R. Lehoux, H. Wang, *Can. J. Chem. Eng.* **2021**, *98*, 153.
[26] M. Norouzi Banis, Z. Wang, S. Rousselot, Y. Liu, Y. Hu, M. Talebi-Esfandarani, T. Bibienne, M. Gauthier, R. Li, G. Liang, M. Dollé, P. Sauriol, T.-K. Sham, X. Sun, *Can. J. Chem. Eng.* **2019**, *97*, 2211.
[27] G. S. Patience, J. Chaouki, M. Latifi, M. Dollé, P. Chartrand, W. Kasprzak, X. Sun, T.-K. Sham, G. Liang, P. Sauriol, *Can. J. Chem. Eng.* **2019**, *97*, 2189.
[28] J. Lee, D. A. Kitchaev, D.-H. Kwon, C.-W. Lee, J. K. Papp, Y.-S. Liu, Z. Lun, R. J. Clément, T. Shi, B. D. McCloskey, J. Guo, M. Balasubramanian, G. Ceder, *Nature* **2018**, *556*, 185.
[29] Z. Chen, Y. Song, J. Cai, X. Zheng, D. Han, Y. Wu, Y. Zang, S. Niu, Y. Liu, J. Zhu, X. Liu, G. Wang, *Angew. Chem. Int. Edit.* **2018**, *57*, 5076.

[30] T. T. H. Hoang, S. Verma, S. Ma, T. T. Fister, J. Timoshenko, A. I. Frenkel, P. J. A. Kenis, A. A. Gewirth, *J. Am. Chem. Soc.* **2018**, *140*, 5791.
[31] M. O. Guerrero-Pérez, *Catalysts* **2018**, *8*, 564. https://doi.org/10.3390/catal8110564.
[32] M. O. Guerrero-Pérez, *Catal. Today* **2017**, *285*, 226. https://doi.org/10.1016/j.cattod.2017.01.037.
[33] R. López-Medina, M. O. Guerrero-Pérez, M. A. Bañares, *New J. Chem.* **2019**, *43*, 17661.
[34] P. Mars, D. W. van Krevelen, *Chem. Eng. Sci.* **1954**, *3*, 41.
[35] C. Doornkamp, V. Ponec, *J. Mol. Catal. A-Chem.* **2000**, *162*, 19.
[36] A. Iglesias-Juez, M. V. Martínez-Huerta, E. Rojas-García, J.-M. Jehng, M. Bañares, *J. Phys. Chem. C* **2018**, *122*, 1197.
[37] M. V. Martínez-Huerta, J. M. Coronado, M. Fernández-García, A. Iglesias-Juez, G. Deo, J. L. G. Fierro, M. A. Bañares, *J. Catal.* **2004**, *225*, 240.
[38] M. V. Martínez-Huerta, G. Deo, J. L. G. Fierro, M. A. Bañares, *J. Phys. Chem. C* **2007**, *111*, 18708.
[39] D. D. Beck, T. W. Capehart, R. W. Hoffman, *Chem. Phys. Lett.* **1989**, *159*, 205.
[40] A. V. Soldatov, T. S. Ivanchenko, S. D. Longa, A. Kotani, Y. Iwamoto, A. Bianconi, *Phys. Rev. B* **1994**, *50*, 5074.
[41] M. A. Bañares, I. E. Wachs, *J. Raman Spectrosc.* **2002**, *33*, 359.
[42] P. Kumar, Y. Jeong, S. Gautam, H. Ha, K. Lee, K. Chae, *Chem. Eng. J.* **2015**, *275*, 142.
[43] H. Murayama, D. Vitry, W. Ueda, G. Fuchs, M. Anne, J. Dubois, *Appl. Catal. A-Gen.* **2007**, *318*, 137.
[44] M. O. Guerrero-Pérez, R. López-Medina, E. Rojas-García, M. A. Bañares, *Catal. Today* **2019**, *336*, 210. https://doi.org/10.1016/j.cattod.2017.12.016.
[45] F. Cavani, N. Ballarini, A. Cericola, *Catal. Today* **2007**, *127*, 113.
[46] A. Iglesias-Juez, A. M. Beale, K. Maaijen, T. C. Weng, P. Glatzel, B. M. Weckhuysen, *J. Catal.* **2010**, *276*, 268.
[47] M. Teliska, W. E. O'Grady, D. E. Ramaker, *J. Phys. Chem. B* **2005**, *109*, 8076.
[48] E. Bus, D. E. Ramaker, J. A. van Bokhoven, *J. Am. Chem. Soc.* **2007**, *129*, 8094.
[49] O. V. Safonova, M. Tromp, J. A. van Bokhoven, F. M. F. de Groot, J. Evans, P. Glatzel, *J. Phys. Chem. B* **2006**, *110*, 16162.
[50] K. Asakura, T. Kubota, W. J. Chun, Y. Iwasawa, K. Ohtani, T. Fujikawa, *J. Synchrotron Radiat.* **1999**, *6*, 439.
[51] E. Castillejos-López, G. Agostini, M. D. Michel, A. Iglesias-Juez, B. Bachiller-Baeza, *ACS Catal.* **2017**, *7*, 796.
[52] A. Iglesias-Juez, A. Kubacka, M. Fernández-García, M. D. Michiel, M. A. Newton, *J. Am. Chem. Soc.* **2011**, *133*, 4484.
[53] D. Bazin, J. J. Rehr, *J. Phys. Chem. B* **2003**, *107*, 12398.
[54] J. Wang, Q. Wang, X. Jiang, Z. Liu, W. Yang, A. I. Frenkel, *J. Phys. Chem. C* **2015**, *119*, 854.
[55] A. L. Bugaev, A. A. Guda, K. A. Lomachenko, V. V. Srabionyan, L. A. Bugaev, A. V. Soldatov, C. Lamberti, V. P. Dmitriev, J. A. van Bokhoven, *J. Phys. Chem. C* **2014**, *118*, 10416.
[56] A. Iglesias-Juez, S. Castellanos, M. Monte, G. Agostini, D. Osadchii, M. A. Nasalevich, J. G. Santaclara, A. I. O. Suarez, S. L. Veber, M. V. Fedin, J. Gascón, *J. Mater. Chem. A* **2018**, *6*, 17318.
[57] M. G. Bakker, B. Fowler, M. K. Bowman, G. S. Patience, *Can. J. Chem. Eng.* **2020**, *98*, 1668.
[58] M. A. Nasalevich, R. Becker, E. V. Ramos-Fernandez, S. Castellanos, S. L. Veber, M. V. Fedin, F. Kapteijn, J. N. H. Reek, J. I. van der Vlugt, J. Gascón, *Energ. Environ. Sci.* **2015**, *8*, 364.
[59] M. A. Nasalevich, C. H. Hendon, J. G. Santaclara, K. Svane, B. van der Linden, S. L. Veber, M. V. Fedin, A. J. Houtepen, M. A. van der Veen, F. Kapteijn, A. Walsh, J. Gascón, *Sci. Rep.* **2016**, *6*, 23676.
[60] P. Reñones, L. Collado, A. Iglesias-Juez, F. E. Oropeza, F. Fresno, V. A. de la Peña O'Shea, *Ind. Eng. Chem. Res.* **2020**, *59*, 9440.
[61] G. L. Chiarello, M. Nachtegaal, V. Marchionni, L. Quaroni, D. Ferri, *Rev. Sci. Instrum.* **2014**, *85*, 074102.
[62] K. Tamura, M. Inui, S. Hosokawa, *Rev. Sci. Instrum.* **1995**, *66*, 1382.
[63] C. Lamberti, C. Prestipino, S. Bordiga, G. Berlier, G. Spoto, A. Zecchina, A. Laloni, F. La Manna, F. D'Anca, R. Felici, F. D'Acapito, P. Roy, *Nuclear Instruments and Methods in Physics Research Section B: Beam Interactions with Materials and Atoms* **2003**, *200*, 196.
[64] P. An, C. Hong, J. Zhang, W. Xu, T. Hu, *J. Synchrotron Radiat.* **2014**, *21*, 165.
[65] J.-D. Grunwaldt, M. Caravati, S. Hannemann, A. Baiker, *Phys. Chem. Chem. Phys.* **2004**, *6*, 3037.
[66] D. Koziej, M. Hübner, N. Barsan, U. Weimar, M. Sikora, J.-D. Grunwaldt, *Phys. Chem. Chem. Phys.* **2009**, *11*, 8620.
[67] M. Louvel, A. Bordage, D. Testemale, L. Zhou, J. Mavrogenes, *Chem. Geol.* **2015**, *417*, 228.
[68] D. Ferri, M. A. Newton, M. D. Michiel, G. L. Chiarello, S. Yoon, Y. Lu, J. Andrieux, *Angew. Chem. Int. Edit.* **2014**, *53*, 8890.
[69] G. L. Chiarello, J. D. Grunwaldt, D. Ferri, F. Krumeich, C. Oliva, L. Forni, A. Baiker, *J. Catal.* **2007**, *252*, 127.
[70] G. L. Chiarello, D. Ferri, J. D. Grunwaldt, L. Forni, A. Baiker, *J. Catal.* **2007**, *252*, 137.
[71] Q. Wu, L. D. L. Duchstein, G. L. Chiarello, J. M. Christensen, C. D. Damsgaard, C. F. Elkjær, J. B. Wagner, B. Temel, J. Grunwaldt, A. D. Jensen, *ChemCatChem* **2014**, *6*, 301.
[72] A. Gaur, M. Schumann, K. V. Raun, M. Stehle, P. Beato, A. D. Jensen, J.-D. Grunwaldt, M. Høj, *ChemCatChem* **2019**, *11*, 4871.
[73] D. Ferri, M. S. Kumar, R. Wirz, A. Eyssler, O. Korsak, P. Hug, A. Weidenkaff, M. A. Newton, *Phys. Chem. Chem. Phys.* **2010**, *12*, 5634.
[74] S. Bordiga, E. Groppo, G. Agostini, J. A. V. Bokhoven, C. Lamberti, *Chem. Rev.* **2013**, *113*, 1736.
[75] D. E. Ramaker, D. C. Koningsberger, *Phys. Chem. Chem. Phys.* **2010**, *12*, 5514.
[76] M. Teliska, W. E. O'Grady, D. E. Ramaker, *J. Phys. Chem. B* **2004**, *108*, 2333.
[77] F. Scott, S. Mukerjee, D. E. Ramaker, *J. Electrochem. Soc.* **2007**, *154*, A396.
[78] D. Ferri, M. A. Newton, M. Nachtegaal, *Top. Catal.* **2011**, *54*, 1070.
[79] G. L. Chiarello, D. Ferri, *Phys. Chem. Chem. Phys.* **2015**, *17*, 10579.
[80] A. Urakawa, T. Bürgi, A. Baiker, *Chem. Eng. Sci.* **2008**, *63*, 4902.

[81] D. Ferri, M. A. Newton, M. D. Michiel, S. Yoon, G. L. Chiarello, V. Marchionni, S. K. Matam, M. H. Aguirre, A. Weidenkaff, F. Wen, J. Gieshoff, *Phys. Chem. Chem. Phys.* **2013**, *15*, 8629.
[82] J. Lefebvre, F. Galli, C. L. Bianchi, G. S. Patience, D. C. Boffito, *Can. J. Chem. Eng.* **2019**, *97*, 2588.
[83] G. L. Chiarello, Y. Lu, M. Agote-Aràn, R. Pellegrini, D. Ferri, *Catalysts* **2021**, *11*, 116.
[84] H. Funke, A. C. Scheinost, M. Chukalina, *Phys. Rev. B* **2005**, *71*, 094110.
[85] J. Timoshenko, A. Kuzmin, *Comput. Phys. Commun.* **2009**, *180*, 920.
[86] M. V. Dozzi, G. L. Chiarello, M. Pedroni, S. Livraghi, E. Giamello, E. Selli, *Appl. Catal. B-Environ.* **2017**, *209*, 417.
[87] M. Muñoz, P. Argoul, F. Farges, *Am. Mineral.* **2003**, *88*, 694.
[88] E. K. Dann, E. K. Gibson, C. R. A. Catlow, V. Celorrio, P. Collier, T. Eralp, M. Amboage, C. Hardacre, C. Stere, A. Kroner, A. Raj, S. Rogers, A. Goguet, P. P. Wells, *J. Catal.* **2019**, *373*, 201.
[89] S. W. T. Price, K. Ignatyev, K. Geraki, M. Basham, J. Filik, N. T. Vo, P. T. Witte, A. M. Beale, J. F. W. Mosselmans, *Phys. Chem. Chem. Phys.* **2015**, *17*, 521.
[90] M. Fialin, C. Wagner, M.-L. Pascal, *Mineral. Mag.* **2011**, *75*, 347.
[91] S. D. M. Jacques, O. Leynaud, D. Strusevich, P. Stukas, P. Barnes, G. Sankar, M. Sheehy, A. Beale, M. O'Brien, A. Iglesias-Juez, *Catal. Today* **2009**, *145*, 204.
[92] L. Bertrand, S. Bernard, F. Marone, M. Thoury, I. Reiche, A. Gourrier, P. Sciau, U. Bergmann, *Top. Curr. Chem.* **2016**, *374*, 7.
[93] M. Favaro, H. Xiao, T. Cheng, W. A. Goddard 3rd., J. Yano, E. J. Crumlin, *P. Natl. Acad. Sci. U.S.A.* **2017**, *114*, 6706.
[94] I. Ascone, R. Strange, *J. Synchrotron Radiat.* **2009**, *16*, 413.
[95] F. Champloy, K. Gruber, G. Jogl, C. Kratky, *J. Synchrotron Radiat.* **2000**, *7*, 267.
[96] S. Wherland, I. Pecht, *Proteins* **2018**, *86*, 817.
[97] G. La-Penna, M. S. Li, *Chem.-Eur. J.* **2018**, *24*, 5259.
[98] F. Arrigoni, T. Prosdocimi, L. Mollica, L. De Gioia, G. Zampella, L. Bertini, *Metallomics* **2018**, *10*, 1618.
[99] V. M. Jiménez, A. Caballero, A. Fernández, J. C. Sánchez-Lopez, A. R. González-Elipe, J. Trigo, J. M. Sanz, *Surf. Interface Anal.* **1997**, *25*, 707.

How to cite this article: A. Iglesias-Juez, G. L. Chiarello, G. S. Patience, M. O. Guerrero-Pérez, *Can. J. Chem. Eng.* **2021**, 1. https://doi.org/10.1002/cjce.24291